Ionization energy of rubidium Rydberg atoms in strong crossed electric and magnetic fields

G. Raithel and H. Walther
Max-Planck-Institut für Quantenoptik and Sektion Physik der Universitat München, D-85748 Garching, Federal Republic of Germany
(Received 20 January 1993)

This paper describes the determination of the ionization threshold of rubidium Rydberg atoms in crossed electric and magnetic fields. An experimental setup is used that allows one to count separately Rydberg atoms which ionize in the region of optical excitation, and those which leave the excitation region in a bound state. The obtained spectra allow one to determine the energy and the width of the ionization threshold. For different values of the electric-field strength E the influence of the magnetic field B on the ionization threshold was investigated. It was found that the scaled electric field $\epsilon = EB^{-4/3}$ and the scaled energy $\omega = WB^{-2/3}$ with excitation energy W are sufficient in order to describe the observed ionization threshold. This is remarkable since ϵ and ω are the classical parameters of the system. For $\epsilon \gtrsim 1.5$ (atomic units), i.e., a weak magnetic field, the ionization energy does not depend on B and can be explained classically by direct-path ionization. In the regime $1.5 \geq \epsilon \geq 0.2$, the energy and the width of the ionization threshold increase with increasing magnetic-field strength. In that regime the observed ionization behavior is qualitatively consistent with the assumption that the excited states are coupled to the continuum via free-electron states which exist at and beyond the classical ionization saddle point, those states corresponding to classical drift trajectories. At $\epsilon \approx 0.2$, the ionization energy takes a maximum value, and in the range $0.2 \geq \epsilon \geq 0.06$, with increasing magnetic field, both the energy and the width of the ionization threshold decrease again. A further increase of the magnetic-field strength changes the tendency a second time: for $\epsilon < 0.06$, both the ionization energy and the width increase again. In this high-magnetic-field regime the ionization energy was explained by classical drift trajectories which almost completely surround the Coulomb center and extend into the continuum. Wave functions of corresponding drift states were calculated using a Born-Oppenheimer approximation. The coupling between the inner-configuration-space volume and the drift states, which leads to ionization, vanishes in the classical limit.

PACS number(s): 32.60.+i, 32.30.Jc, 32.80.Fb

I. INTRODUCTION

In recent years, Rydberg atoms in strong static external fields have attracted much interest since the classical dynamics of hydrogenic systems gets chaotic in strong magnetic fields [1–3]. Rydberg atoms in either strong magnetic fields or in crossed electric and magnetic fields are very well suited for theoretical as well as experimental investigations of the question of how classical chaos manifests itself in corresponding quantum systems. The Hamiltonian of hydrogen Rydberg atoms in a strong magnetic field is comparatively simple due to its time independence and its conservation of l_z. ([1–3], and references therein). Thus from the theoretical point of view this system is ideal for the study of both classical chaos and quantum mechanical behavior. As a consequence, there were extensive theoretical investigations of atoms in strong magnetic fields, most of them being done on atomic hydrogen. (See Ref. [4] for a review.) Positive energy spectra of Rydberg atoms in strong magnetic fields were also calculated using the complex-rotation method [5] and the R-matrix formalism [6]. Positive energy spectra of lithium Rydberg atoms in strong magnetic fields were calculated and compared with experimental results using the diabatic-by-sector method [7]. The same experimental results could be theoretically reproduced by a combination of complex-rotation and R-matrix methods [8]. The complex-rotation method was also extended to crossed fields [9]. There were also many experiments on Rydberg atoms in strong magnetic fields (as well as in crossed fields) utilizing high-resolution laser spectroscopy ([10–13], and references therein). Highly resolved spectra of Li above the zero field ionization energy were recorded by Kleppner and co-workers [14].

There are significant changes in the excitation spectra as these systems enter the chaotic regime. The nearest neighbor distribution of the energy levels was found to evolve from a Poisson distribution to a Wigner distribution when increasing the influence of the magnetic field [2,3]. The overall structure of the excitation spectra of Rydberg atoms in strong magnetic fields also exhibits a prominent change already observed in 1969: in the high-magnetic-field regime, i.e., in the classically chaotic regime, the excitation spectra of Rydberg atoms exhibit sinusoidal modulations which are absent in the low-magnetic-field regime [15]. Since the spacing of the modulations was close to the electron cyclotron frequency, these resonances were called quasi-Landau (QL) resonances. Different types of such QL resonances were observed in magnetic fields as well as in crossed electric and magnetic fields [10–13]. The QL resonances are analyzed best by a Fourier analysis of the scaled spectra which are measured by changing the external field values as a function of the excitation energy. This procedure is described

in detail in Ref. [13]. In the case of crossed fields, the scaled spectroscopy utilizes a classical scaling property of the hydrogen atom: the classical dynamics is solely determined by the scaled electric field $\epsilon = EB^{-4/3}$ and the scaled energy $\omega = WB^{-2/3}$ (with energy W, electric field E, and magnetic field B). These scaled parameters will be thoroughly used in this paper. It was first recognized by Edmonds and Starace [16,17] that the QL resonances are associated with classical closed trajectories of the system. In Refs. [10,11,18,19,13] many types of QL resonances are related to classical recurring trajectories. A formalism describing the QL resonances was developed by Du and Delos [20,21] which found a quantitative expression allowing one to calculate the modulation strengths of different classical orbits. Following Gutzwiller, who found a semiclassical approximation of the level density ([22], and references therein), they employed a semiclassical approximation of the Green's function.

With methods similar to that employed in [20–22], other authors investigated the influence of classical trajectories on wave functions [23–26]. For a chaotic billiard system, Bogomolny derived a semiclassical approximation for probability distributions slightly averaged over energy and space, this approximation consisting of a mean part plus a sum over all periodic orbits. A wave function may be strongly enhanced along one single orbit. This "scarring" phenomenon was investigated by Wintgen and Hoenig [26] for diamagnetic hydrogen. The theoretical work suggests that properties of Rydberg atoms depending on the charge distribution of the Rydberg electron may be explained by recurring trajectories: in Ref. [27], the electric dipole moments of Rydberg atoms in crossed electric and magnetic fields were measured, and the observed dipole moments were explained by classical orbits.

One of the most fundamental properties of a system is its ionization energy. In this paper the ionization threshold of rubidium Rydberg atoms in crossed fields is investigated in detail experimentally. With a sensitive experimental setup, described in Sec. II, it was possible to detect separately excited atoms which are not ionized by the fields present in the excitation region, and those which are ionized at or close to the excitation point. Since it is possible to take simultaneously two separate spectra—one for Rydberg atoms living longer than roughly 20 μs after the excitation, and one for atoms which ionize during that time—both the energy and the width of the ionization threshold can be accurately measured. The experimental results are presented in Sec. III where it is also shown that the energy and the width of the ionization threshold follow the classical scaling laws to a good approximation. Starting from classical considerations in Sec. IV, the experimental results are explained in the framework of a Born-Oppenheimer approximation of the Schrödinger equation. The obtained wave functions are located on shells around the Coulomb center which couple the excited Rydberg states to the continuum and thus lead to ionization.

II. EXPERIMENTAL SETUP

The experimental setup, which is similar to that described in Ref. [13], is sketched in Fig. 1. A beam of rubidium atoms effusing from an atomic beam oven (nozzle diameter ≈ 0.3 mm) enters a field region providing homogeneous crossed electric and magnetic fields, the latter being parallel to the atomic beam direction. The Rydberg atoms are excited by 297 nm UV laser radiation in one step. Owing to the good collimation of the atomic beam, Doppler-free spectra are obtained. A superconducting magnet yields a magnetic-field strength of up to 6 T at the excitation point. The strong magnetic field is also used to image the signal electrons onto the surface of a microchannel-plate (MCP) detector. The homogeneous electric field at the excitation point is produced by field electrodes, which also help to provide a controllable motion of the electrons resulting from atoms which are directly photoionized in the excitation region. Stable

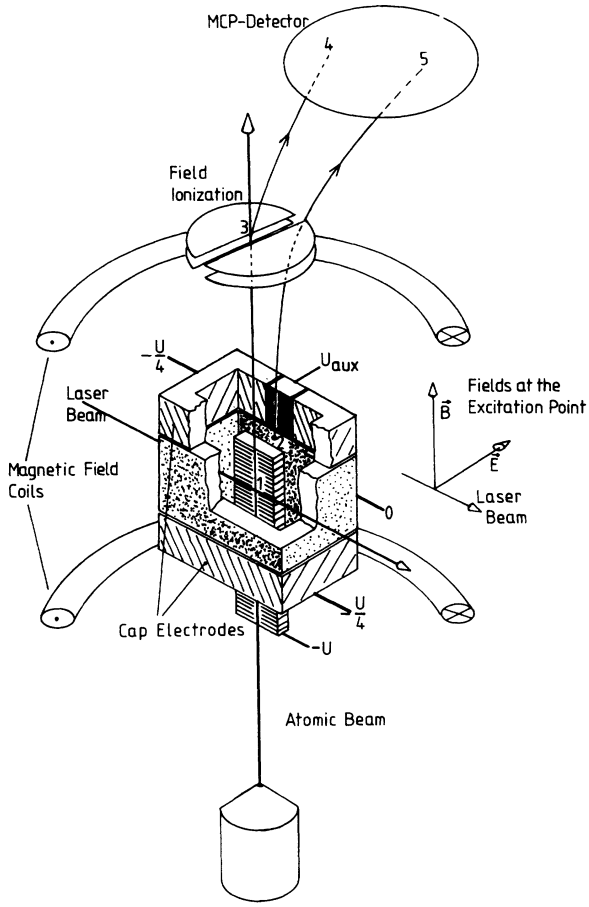

FIG. 1. Sketch of the experimental setup. A thermal beam of rubidium atoms is excited at the excitation point (1) by 297 nm laser light. The field directions at the excitation point are indicated in the inset. The electric-field electrodes provide a homogeneous electric field in the excitation region and lead to controllable motion of the electrons resulting from direct photoionization. The cap electrodes prevent the photoelectrons from escaping in magnetic-field direction. Rydberg atoms which are not photoionized are field ionized at point (3) and the electrons are detected by the microchannel plate (MCP) around point (4). Due to the influence of the auxiliary electrode which is on the positive voltage U_{aux} electrons originating from photoionized atoms leave the electron trap at point (2), and give a signal at location (5) on the detector.

Rydberg atoms are field ionized and detected downstream after they have left the interaction region. Rydberg atoms ionizing in the excitation region leave an electron within the electrode arrangement which has a very low kinetic energy (in the meV range). The kinetic energy is composed of a vertical part and a horizontal part, the latter being normal to the vertical magnetic field. The horizontal motion is an $\mathbf{E}\times\mathbf{B}$ drift motion, i.e., the electron moves perpendicular to the average horizontal electric-field component, the average taken over one of the vertical oscillations depicted in Fig. 2. These oscillations arise from the repulsive force produced by the cap electrodes in vertical direction. Due to the low electron energy the electrons do not penetrate deeply into the repulsive zone. The action of the fields is very similar to a Penning trap. During the vertical oscillations the electrons simultaneously perform the transverse drift motion and approach the auxiliary electrode (see Figs. 1 and 2) which exerts an attractive force on the electrons. The vertical component of this force extracts the electrons out of the trap, whereas the component of the attractive force perpendicular to the magnetic field only slightly changes the electron energy transverse to the magnetic-field direction. Once the electrons gained kinetic energy in magnetic-field direction, they essentially move parallel to the magnetic field, unaffected by moderate transverse electric fields (Fig. 1). In effect, the magnetic stray field images the location where the electrons leave the trap region onto the MCP detector. On the MCP surface, there are two well resolved spots where electrons are detected: one spot corresponding to atoms which have already been photoionized in the excitation region, and another spot for Rydberg atoms which are ionized in the field ionization region. Figure 3 shows an image which is obtained by integrating the signal for a few minutes. By defining two suitable spatial counting windows, separate excitation spectra for stable Rydberg atoms and photoionized atoms can be obtained.

Since the apparatus utilizes the $\mathbf{E}\times\mathbf{B}$ drift motion it only works well if the magnetic field exceeds about 0.1 T. If the magnetic field gets weaker, two disturbing effects occur: the size of the cyclotron radius of the drifting electrons gets larger, and the drift velocity E/B becomes important, especially in the field ionization region where the magnetic-field strength has already decreased considerably. Nevertheless, the field range where the apparatus works well is very large (about 0.2 to 6 T with electric fields between 10^3 and 10^5 V/m). Thus, besides ordinary spectra taken at constant field values, it is also no problem to take scaled spectra as described in Ref. [13]. Scaled spectra can also be measured in the continuum; this is planned to be the subject of a future paper.

An important time scale of the apparatus is the time of flight of the excited atoms through the electric field in the excitation region. From the atomic velocity ($\approx$400 m/s) and the path length of the atoms traversed within the excitation electric field ($\approx$8 mm) this time scale becomes $\approx$20 μs, which is five to six orders of magnitude longer than the revolution time of the most prominent quasi-

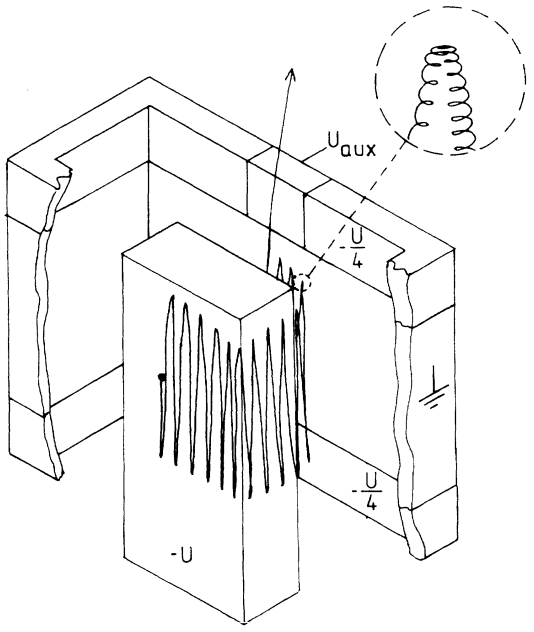

FIG. 2. Electron drift motion of the photoelectrons in the trap region (qualitatively). The electrode orientation relative to atomic beam, laser beam, and magnetic field can be easily recognized by comparison with Fig. 1. The cap potential $-U/4$ prevents the electrons from escaping in the direction of the magnetic field. As the electron approaches the auxiliary electrode which is on the positive voltage U_{aux} the electron is extracted from the trap. The enlarged inset shows the electron micromotion at an upper turning point. The insulating gaps between the outer electrodes are merely indicated by lines in this figure.

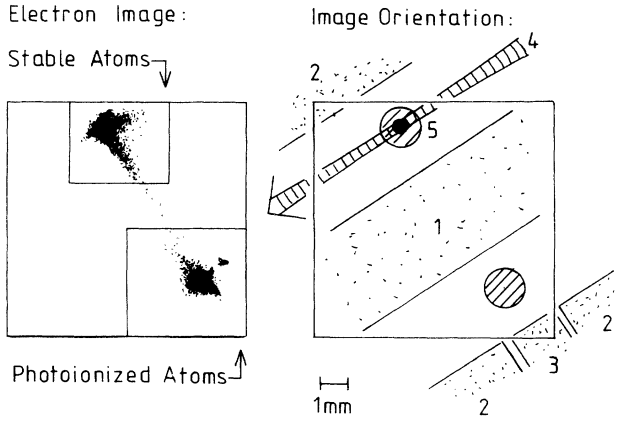

FIG. 3. The left part of the figure shows a spatially resolved electron image measured by the MCP detector. The applied fields and the excitation energy are chosen in a way which provides comparable numbers of photoionized atoms and atoms ionized in the field ionization zone. By counting into two channels associated with the windows indicated in the image one gets separate spectra for stable and photoionized Rydberg atoms. The orientation of the image with respect to the electrode arrangement is visualized in the right part of the figure. The indicated length of 1 mm corresponds to the size of the electron image at the field ionization zone (see Fig. 1). [(1) inner electrode, (2) cap electrode, (3) auxiliary electrode, (4) laser beam, (5) atomic beam.]

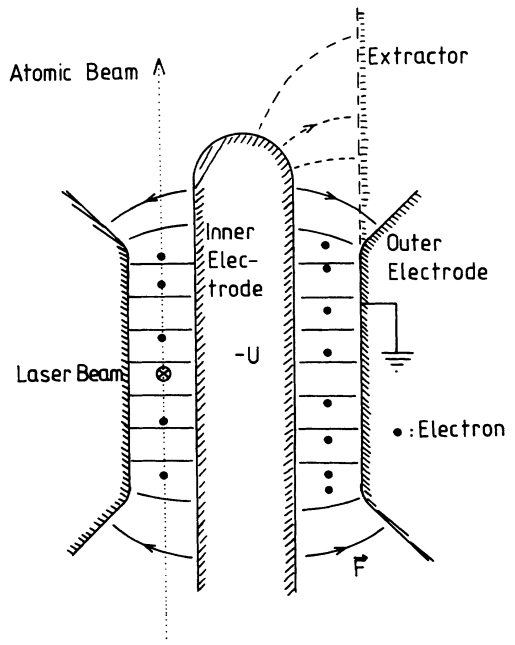

FIG. 4. Electrode geometry avoiding strong electric fields at the trap periphery. The displayed arrangement has the additional advantage that only one nonzero potential is required. The electrons (represented by thick dots) are trapped via the vertical force component being present in the outer, inhomogeneous part of the electric field. For the extraction of the photoelectrons the outer electrode is extended on one side as indicated by the dashed line.

Landau orbits [13]. If the lifetime of the Rydberg atoms with respect to field ionization in the excitation region is about 20 μs the counting rates in the two windows are comparable (as realized, for example, in Fig. 3). Thus the critical lifetime which defines the ionization threshold in this experimental setup is 20 μs.

The electrode geometry presented in Fig. 1 generates an electric field in the cap region which is parallel to the magnetic field. If the atomic beam is not well aligned, and passes too close to the cap electrode, Rydberg atoms may ionize. The associated field ionization electrons at least partially reach the detector within the photoionization counting window. This phenomenon leads to wrong results for the ionization threshold. In order to avoid this effect the atomic beam has to be well aligned. Additionally the cap potential has been chosen as close to zero as possible. The potential step can be avoided completely by an electrode geometry shown in Fig. 4 which has been used as a good alternative in some of the experiments. However, most of the experimental results presented in this paper have been obtained with the setup shown in Fig. 1. Some test experiments with the geometry shown in Fig. 4 have confirmed that the presented experimental results are not influenced by the cap potentials of the originally chosen setup (Fig. 1).

III. EXPERIMENTAL RESULTS

A. Excitation spectra and fractional ionization probability

With the described setup the ionization energy and the width of the ionization threshold were measured as a function of E and B. Different sets of spectra were recorded, each set characterized by a different electric-field value E. Each set consists of spectra taken at different values of the magnetic-field strength B, i.e., different scaled electric-field values ϵ. During the scan of the laser frequency across the ionization threshold two spectra were simultaneously recorded, one spectrum for the stable Rydberg atoms, and the other for photoionized rubidium atoms. Figures 5 and 6 show the results for electric fields of $E=9\times10^3$ V/m and $=3\times10^3$ V/m, respectively.

The first important observation is that the sum counting rate (stable atoms plus photoionized atoms) does not change significantly when passing the ionization threshold. Since the energy-averaged oscillator strength does not change strongly at the ionization threshold it can be concluded that the photoionization events are recorded with the same counting efficiency as the stable Rydberg atoms. The long zero traces in Figs. 5 and 6 right or left of the ionization threshold additionally show that there are only a few dark counts and only a small number of events which are counted in the wrong channel; the latter result mainly from imperfections in the imaging fields.

If $N_{\rm ion}$ is the number of counts in a certain channel of the photoionization spectrum, and $N_{\rm at}$ is the number of counts in the same channel of the excitation spectrum of the stable Rydberg atoms, the fractional ionization probability $P_{\rm ion}$ is given by

$$P_{\rm ion}=\frac{N_{\rm ion}}{N_{\rm ion}+N_{\rm at}} . \tag{1}$$

This holds since two associated data points were actually taken simultaneously, i.e., without intermediate laser or field tuning. Figures 7 and 8 show the values of $P_{\rm ion}$ derived from the data displayed in Figs. 5 and 6. While scanning the excitation energy it may happen that the total counting rate approaches zero (in particular for small scaled electric-field strength). Equation (1) shows that in this case even a few spurious counts in the large counting window for the ionized Rydberg atoms appear as large ionization probabilities. By visual inspection it can be recognized that the large "spikes" in Figs. 7 and 8 indeed occur if the total counting rate approaches zero. The actual fractional ionization probability is the lower envelope of the curves plotted in Figs. 7 and 8.

B. The ionization energy

We first turn to the discussion of the ionization energy itself, a reasonable definition of which is that 50% of the atoms are photoionized. This definition depends on the interaction time of the excited atoms with the field region which in our case is $\approx$20 μs. However, the average lifetime of the excited Rydberg states decreases rapidly with increasing excitation energy, as follows from the small width of the ionization threshold. Thus results obtained with a different interaction time would only be shifted with respect to our results, but the interpretations (Sec. IV) would be the same.

Figures 5–8 clearly show that the ionization threshold does not follow the naive expectation at all: whereas one

is tempted to assume that the magnetic field should stabilize the atoms with respect to field ionization, the experiments reveal that at $\epsilon \approx 0.2$ the ionization energy passes a pronounced maximum. As the magnetic field is increased the following behavior is found.

(i) For very small magnetic fields ionization occurs if the energy exceeds the energy of the classical ionization saddle point (which will be called "ISP" throughout the paper), $W_{\text{ion}} = -2\sqrt{E}$. This holds for $\epsilon \gtrsim 1.5$, as follows from the spectra shown in this paper, and other spectra which are not presented.

(ii) Following the classical expectation in the range $1.5 \geq \epsilon \geq 0.2$, the ionization energy increases with increasing magnetic field.

(iii) At a certain value of the magnetic field B, the ionization energy W_{ion} takes a maximum value. The values of B and W_{ion} where the maximum is observed depend on the constant electric field E which has been applied.

(iv) If the magnetic field is further increased $(0.2 \geq \epsilon \geq 0.06)$ the ionization energy decreases until a minimum is reached. For each value of the electric field E, the ionization energy minimum is found at well defined values of B, and W_{ion}.

(v) For magnetic fields above the ionization energy minimum ($\epsilon < 0.06$), the ionization energy smoothly increases with the magnetic field. In the experimentally accessible magnetic-field range this second increase does not cease.

The properties of rubidium Rydberg atoms in strong crossed fields can be interpreted semiclassically to a large extent. The question arises of whether the observed ionization curve can be explained semiclassically as well. In order to show that this assumption is reasonable, the value of $(\omega_0 - \omega_{\text{ion}})/\omega_0$ was plotted versus the scaled electric field ϵ, whereby $\omega_{\text{ion}} = W_{\text{ion}} B^{-2/3}$ is the scaled energy of the ionization threshold, and $\omega_0 = -2B^{-2/3}\sqrt{E} = -2\sqrt{\epsilon}$ the scaled energy of the classical ionization saddle point. This plot emphasizes the magnetic-field-induced changes of the ionization energy relative to the magnetic-field-free ionization threshold. Moreover, if the system follows the classical scaling laws, different experiments should give similar plots. Figure 9 shows the result obtained from Figs. 7 and 8: every ionization probability curve of Figs. 7 and 8 corresponds to

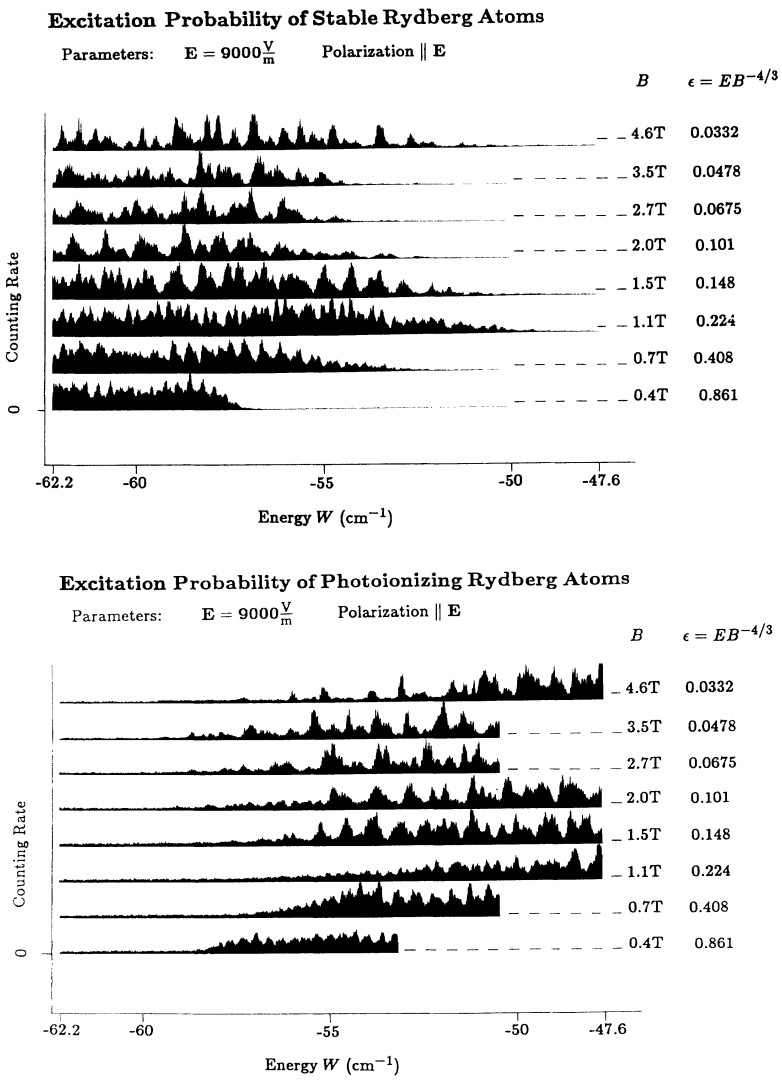

FIG. 5. The upper part of the figure shows spectra obtained by counting into the upper window of Fig. 3, i.e., stable Rydberg atoms are counted. The electric field was kept constant at 9×10^3 V/m. As indicated, the excitation energy W was scanned from -62.2 cm^{-1} up to an energy well above the ionization threshold. The magnetic field and the corresponding scaled electric field ϵ are given for each recording. The lower part of the figure shows the spectra obtained in the lower window of Fig. 3. Upper and lower spectra with equal magnetic-field values were recorded simultaneously. In order to cover all the ionization thresholds associated with the different magnetic-field values, the energy scale has to be rather compressed. This implies that the details of the spectra are obscured to a great extent; one essentially recognizes the ionization thresholds and the quasi-Landau structure in crossed fields, the latter corresponding to the smooth modulations of the spectra. Only a few strong spectral lines can be seen on top of quasi-Landau modulations. The actual resolution of approximately 30 MHz, which is determined by residual electric-field inhomogeneities, would be accurate enough to give much more detailed spectral information. Since only the ionization threshold is of interest here, the spectra have been recorded only at the high energy end of the ionization threshold. Since that energy changes with magnetic field, the spectra are truncated at different energy values.

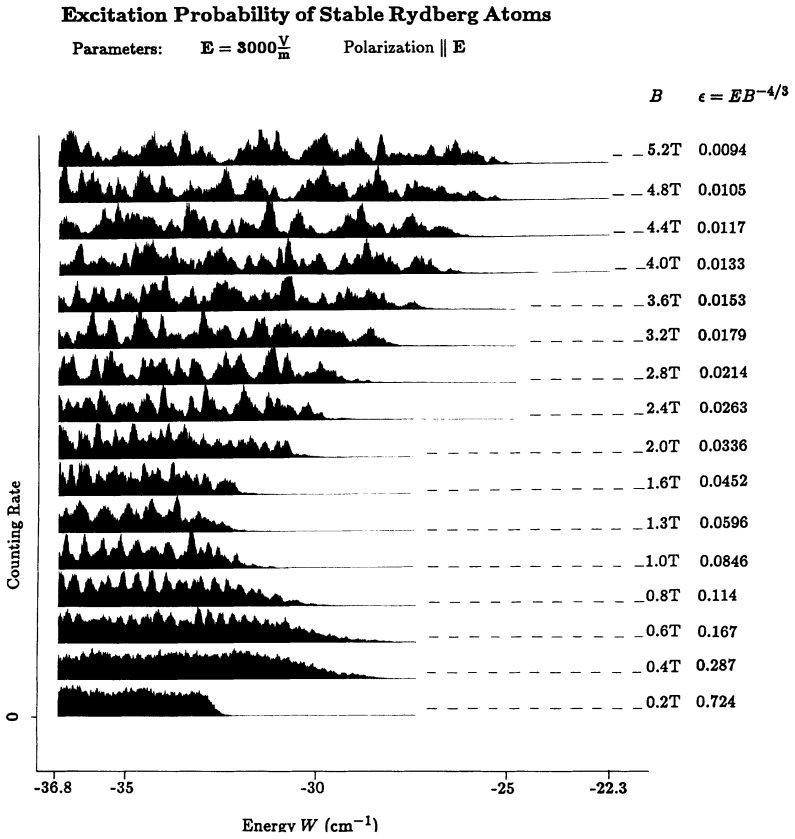

FIG. 6. These spectra are taken at a constant electric field of 3×10^3 V/m. The presentation is analogous to Fig. 5.

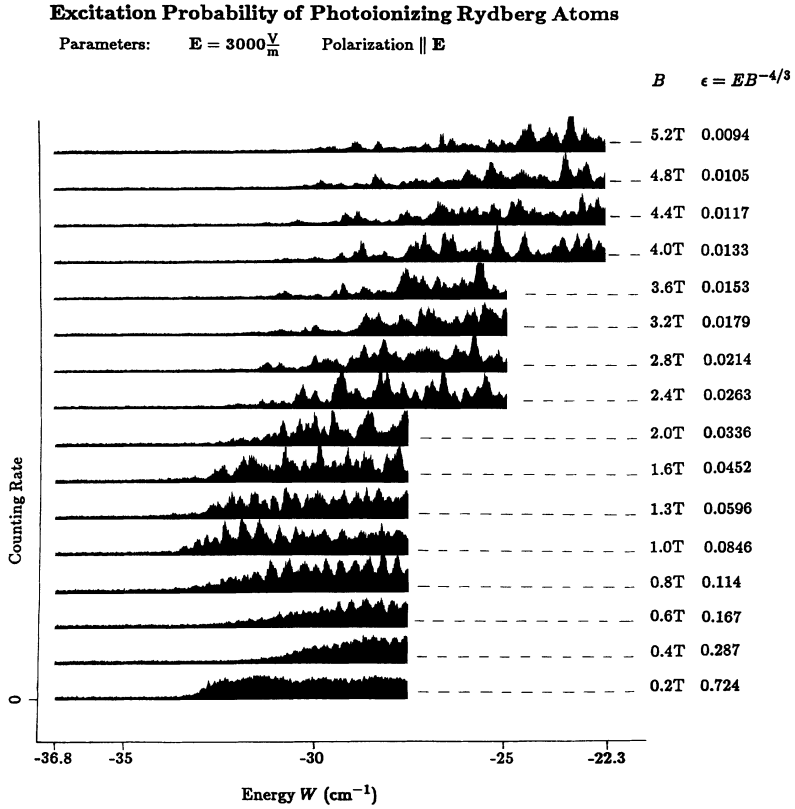

one bar in Fig. 9, the lower bound corresponding to the 20% ionization energy, the circles to the 50%, and the upper bound to the 90% ionization energy. The similarity of the data obtained from Figs. 7 (full circles) and 8 (open circles) clearly indicates that a classical explanation of the ionization behavior should exist.

A classical interpretation of the ionization behavior only makes sense if the two significant points of the ionization curve always occur at the same scaled electric field ϵ and scaled ionization energy ω_{ion}. Figure 10 verifies that actually the ionization energy maximum al-

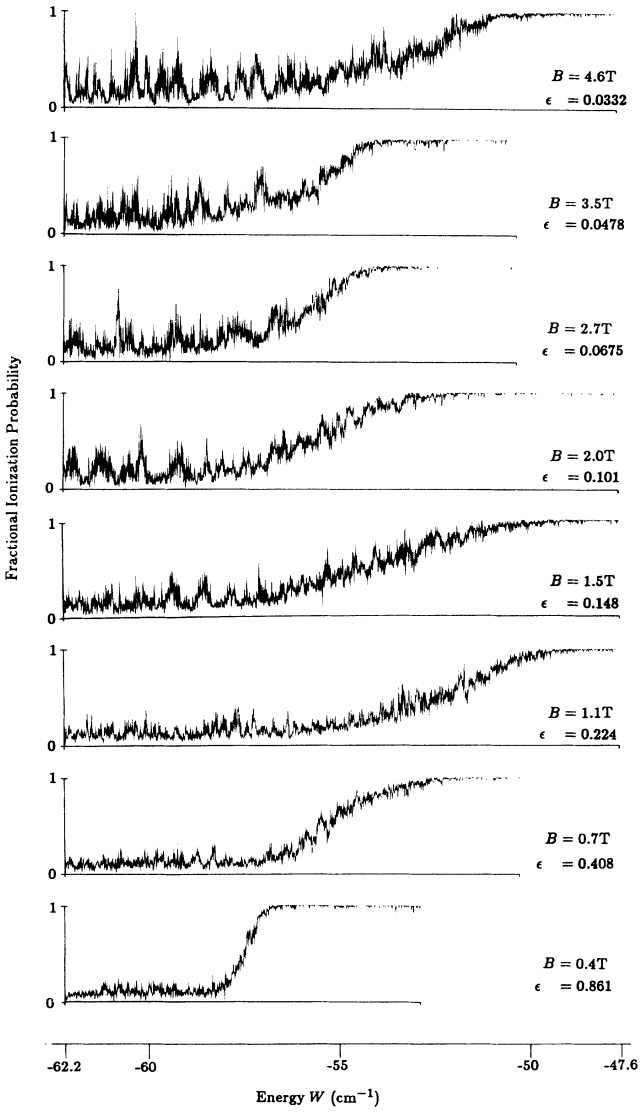

FIG. 7. Fractional photoionization probability as derived from the simultaneously recorded spectra of photoionized and stable Rydberg atoms displayed in Fig. 5 (for details see text). The electric field was $E = 9000$ V/m, and the laser polarization was parallel to the electric field. The "spikes" on the left side of the clearly visible ionization threshold are artifacts generated by spurious counts in the photoionization window. The lower boundary of the displayed lines thus represents the actual fractional ionization probability. The plots in this figure and in Fig. 8 allow one to determine energy and width of the ionization threshold.

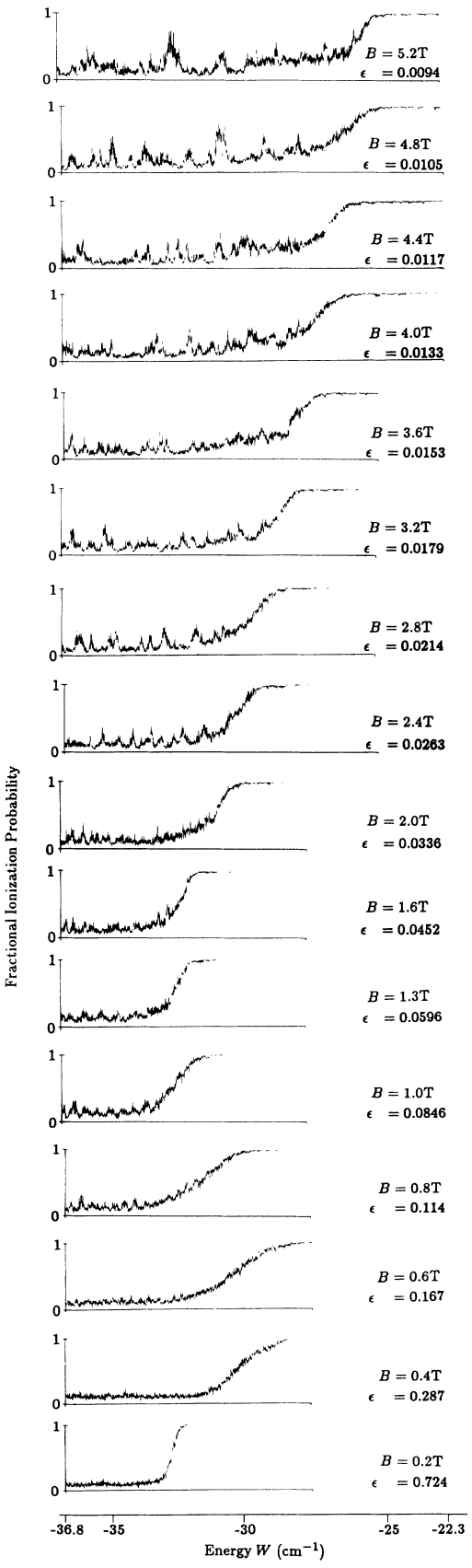

FIG. 8. Fractional photoionization probability as derived from the spectra in Fig. 6. The electric field was $E = 3000$ V/m and the laser polarization was parallel to the electric field.

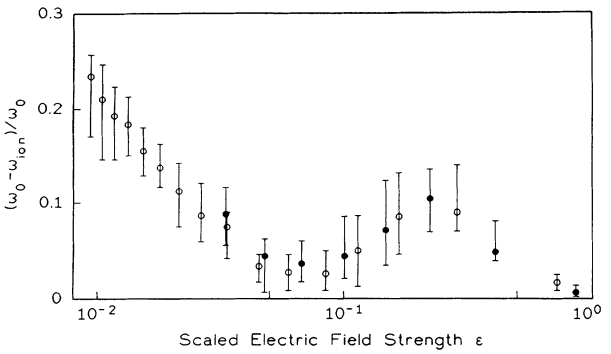

FIG. 9. Ionization energy in scaled variables. The deviation of the scaled ionization energy ω_{ion} from the ISP $\omega_0=-2B^{-2/3}\sqrt{E}$, normalized by ω_0, is plotted versus the scaled electric field ϵ (note the logarithmic scale for ϵ). The filled (open) circles are derived from the 50% ionization energy values in Fig. 7 (Fig. 8). The lower (upper) end of the error bars correspond to the 20% (90%) ionization energy values. Within the experimental accuracy the ionization curve is completely determined by the (classical) scaled parameters. This holds at least for 3×10^3 V/m $\leq E \leq 9\times10^3$ V/m.

ways occurs at $\epsilon=0.19(\pm8\%)$ and $\omega_{ion}=-0.74(\pm6\%)$; similarly in Fig. 11 it is shown that the ionization energy minimum is always found at $\epsilon=0.058(\pm10\%)$ and $\omega_{ion}=-0.45(\pm8\%)$. The measurements of Figs. 5 and 6 and data obtained from additional experiments are included in Figs. 10 and 11. The classical scaling behavior of both ionization energy maximum as well as minimum, which was observed over a wide range of external field values, is another clear hint that a classical explanation of the ionization curve should be possible.

C. The width of the ionization threshold

Figures 7 and 8 also provide information on the width of the ionization threshold which also depends on the scaled electric field. In the high scaled electric-field regime ($\epsilon>1$) the width of the ionization threshold is very small (approximately 2% of the ionization energy $-2\sqrt{E}$). In the vicinity of the ionization energy maximum, the width of the ionization threshold also takes a maximum value. For scaled electric fields $\epsilon<0.06$ the width of the ionization threshold seems to be more or less constant; however, both the original data in Figs. 5 and 6 as well as the ionization probabilities in Figs. 7 and 8 for $\epsilon<0.06$ exhibit two regimes: at low fractional ionization probability P_{ion} (i.e., typically $P_{ion}\leq30-50\%$) the slope dP_{ion}/dW is quite small, contrary to the upper part of the ionization threshold where in general P_{ion} approaches 100% quite rapidly. This behavior indicates that there may be two qualitatively different ways of ionization. If the width of the ionization threshold was measured directly, the information on the presence of two slope regimes for $\epsilon<0.06$ would be lost. Therefore the slope value dP_{ion}/dW was measured, which was taken at $P_{ion}=50\%$ for $\epsilon>0.1$. For $\epsilon<0.07$ the slope of the ionization curve is double-valued, one value taken at $P_{ion}\approx25\%$, the other at $P_{ion}\approx70\%$. Figure 12 shows the values of $2\sqrt{E}\,(dP_{ion}/dW)$ as a function of the scaled electric field. Due to the multiplication with $\sqrt{E}$ different sets of experiments should give the same results if the behavior can be described solely by the scaled parameters ϵ and ω. Figure 12 indicates that this is the case. It is concluded that at least for 3×10^3 V/m $\leq E \leq 9\times10^3$ V/m, not only does the energy of the ionization threshold exhibit classical scaling behavior but also its slope value(s) exhibit this behavior. The explanation of the structure of the ionization threshold needs a fully quantum mechanical treatment, which is not presented in this paper.

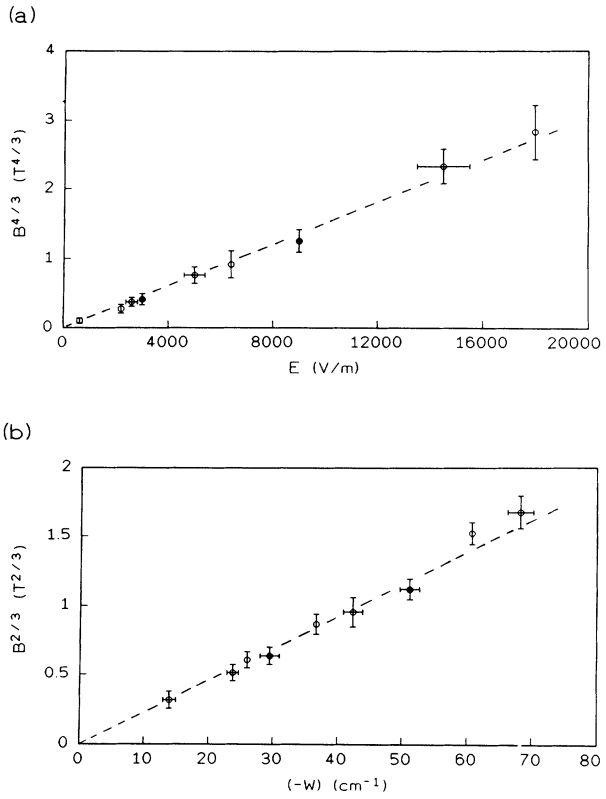

FIG. 10. Scaling behavior of the ionization energy maximum concluded from two different types of measurements. In the first type, the electric field was kept constant and the ionization energy maximum was searched by taking excitation spectra for different magnetic fields. Data points for this type of measurements exhibit negligible errors of the electric field, whereas there are considerable error bars in the magnetic field as well as in the ionization energy. The sets of measurements shown in Figs. 5 and 6 (corresponding to the filled dots in Figs. 10 and 11) belong to that group of measurements. The second type of data points is obtained by taking excitation spectra as a function of the magnetic field with constant excitation energy and different values of the electric field. Consequently these measurements exhibit errors in E and B, and negligible error in W_{ion}. (a) shows that the ionization energy maximum occurs at a scaled electric field $\epsilon=EB^{-4/3}=0.19(\pm8\%)$, that value corresponding to the dashed linear regression curve. Similarly, the linear relation following from (b) allows one to conclude that the scaled ionization energy at the ionization energy maximum is $\omega_{ion}=W_{ion}B^{-2/3}=-0.74(\pm6\%)$.

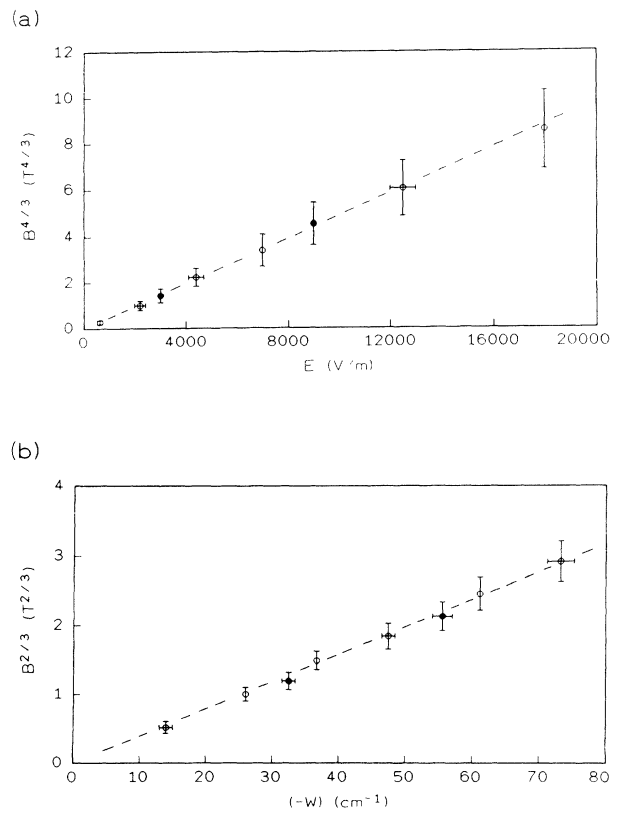

FIG. 11. Investigation of the ionization energy minimum. The diagrams are obtained analogously to the way Fig. 10 was obtained. The scaled parameters of the ionization energy minimum are found to be $\epsilon=0.058(\pm 10\%)$ and $\omega_{\text{ion}}=-0.45(\pm 8\%)$. The errors are larger than in Fig. 10 since in the experimental data the minimum of the ionization energy is not as well defined as the maximum.

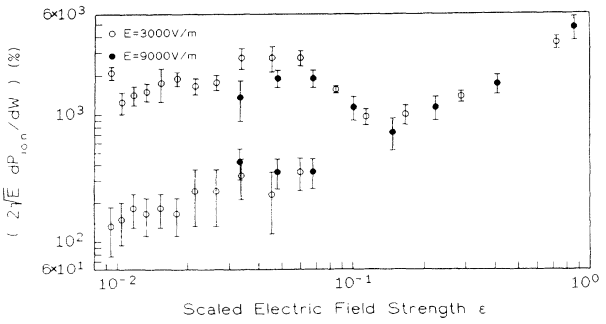

FIG. 12. Slope dP_{ion}/dW of the fractional ionization probability $P_{\text{ion}}(W)$, multiplied by $2\sqrt{E}$, versus the scaled electric field ϵ (double logarithmic plot). When the multiplication by $2\sqrt{E}$ is performed, the data obtained with different electric fields E should yield similar plots if the ionization behavior is determined solely by the classical scaled parameters ϵ and ω. As explained in the text, for small ϵ two values dP_{ion}/dW can be derived from Figs. 7 and 8.

IV. INTERPRETATION OF THE EXPERIMENTAL RESULTS

A. Ionization in the high-magnetic-field regime

1. *The drift trajectories*

In the preceding section new data on the ionization threshold of rubidium in crossed fields are presented. The classical scaling behavior of the results suggests that it should be possible to explain the ionization of Rydberg atoms in crossed fields classically. Though a classical technique cannot give accurate results on ionization rates, the coarse features such as the existence of an intermediate ionization energy minimum at $\epsilon\approx 0.06$ should at least follow from the classical treatment. In this section, the experimental results are interpreted starting from classical trajectory calculations. It will be seen that the main features of the ionization curve can be explained classically, and that the basic principles of the ionization in crossed fields can be understood. The discussion which will be given here can be used as a starting point for future quantum mechanical calculations.

In a classical picture of the ionization process, an electron is launched from the core with an energy above the ionization threshold and disappears in the continuum. In order to find the ionization energy one has to determine the energy above which this direct-path ionization is possible. With trajectory calculations one easily finds that for the range $\epsilon < 1.5$, the ionization energy resulting from direct-path ionization would by far exceed the actually observed ionization energy. Thus a "more effective" ionization mechanism must exist.

When considering ionization, it is useful to get a feeling on the excited state wave function. Trajectory calculations reveal that in the presence of a magnetic field and a crossed electric field, the classical motion of electrons launched at the Coulomb center in any direction is restricted to a certain inner fraction of the energetically allowed configuration space, i.e., the classical excited electrons do not explore the whole energetically allowed space, but only a fraction limited by a certain surface. With increasing magnetic-field strength, the region which is accessed by classical excited electrons contracts more and more. In the limit $E\rightarrow 0$ the classical excited electrons moves within the well-known cigar-shaped equipotential surface of the diamagnetic potential in the symmetric gauge plus the Coulomb potential. The correspondence between classical trajectories and wave functions (see [23–26]) allows one to conclude that the spatial extension of the excited wave functions coincides to a good approximation with the region occupied by the classical excited electrons.

In the following, a brief empirical discussion of different regimes of the classical dynamics of the system is given. For simplicity we take the external electric field $\mathbf{E}=-E\mathbf{e}_x$ and the magnetic field $\mathbf{B}=B\mathbf{e}_z$. The Hamiltonian in the symmetric gauge is

$$H=\frac{1}{2}p^2+\frac{B}{2}l_z+\frac{B^2}{8}(x^2+y^2)-Ex-\frac{1}{|r|}\ , \qquad (2)$$

where an infinite mass of the Coulomb center has been assumed. Figure 13 shows for different scaled electric-field values two classical trajectories with equal energy, one with the electron launched at the core, and the other with it launched far outside. The energy was approximately the experimentally observed ionization energy. First, the inner trajectories which correspond to classical excited electrons will be discussed. It can clearly be seen that the inner trajectory contracts with decreasing scaled electric field. The dynamics of the inner trajectories is regular for $\omega < -0.5$, whereas the trajectory at $\omega = -0.203$ gets chaotic. This has to be compared to Refs. [2,3], where in the electric-field-free case chaotic motion develops in the range $-0.5 \leq \omega \leq -0.2$. Figure 13 allows the assumption that the additional electric field does not dramatically change the chaos limit.

Now we turn to the discussion of the outer trajectories, where the electron has been launched far from the Coulomb center. For $\epsilon = 0.723$, no basic difference between inner and outer trajectory is evident. Both are regular, and due to the weak influence of the magnetic field there is no magnetic-field-induced limitation of the accessible space region, i.e., the energetically allowed configuration space cannot be divided into different parts which can be exclusively reached by trajectories started at or far off the center. For decreasing ϵ the situation completely changes: whereas the trajectories starting at the Coulomb center are gradually restricted to a small central part of the energetically allowed configuration space, the outer trajectories avoid gradually the vicinity

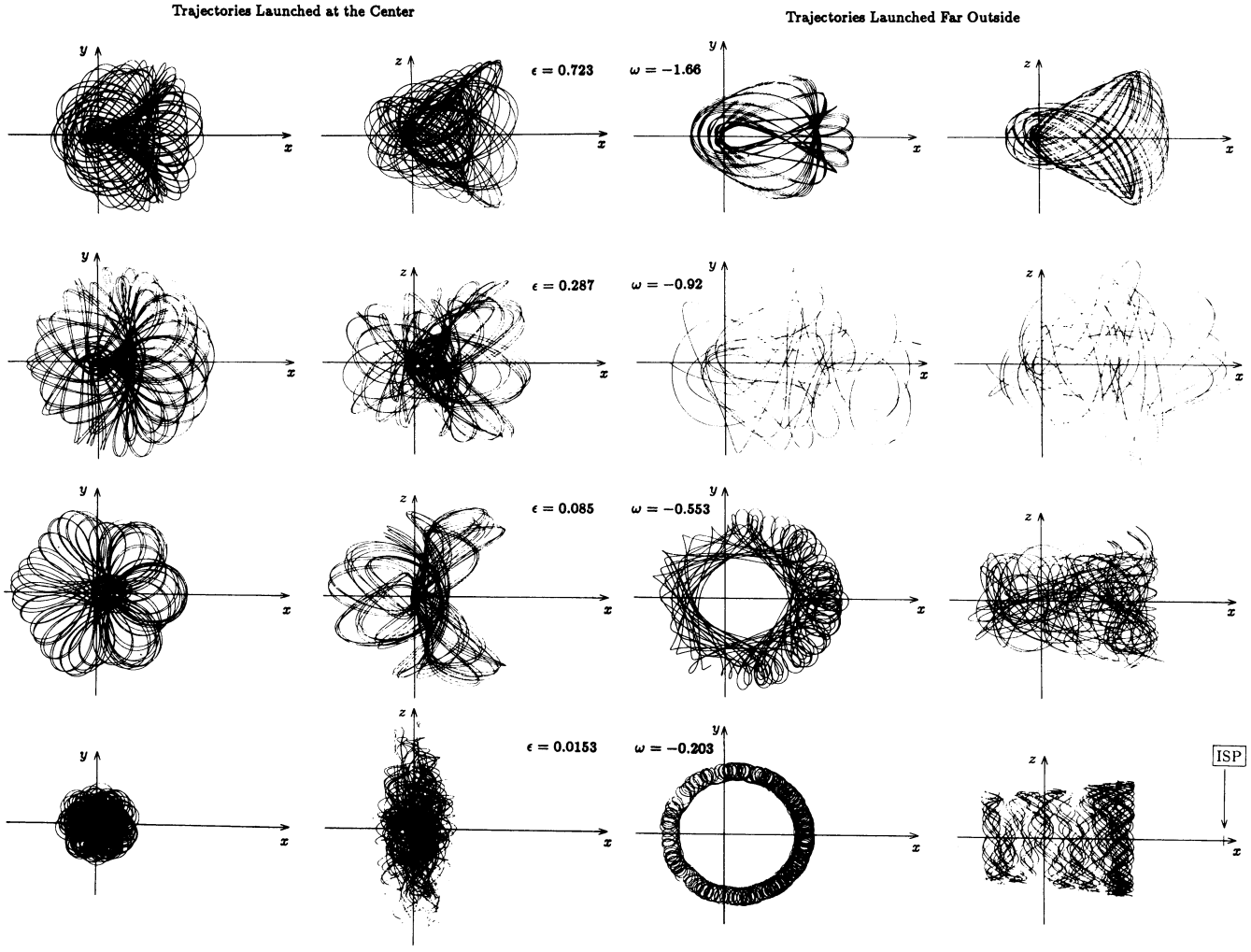

FIG. 13. Trajectories for different values of the scaled electric-field strength at the ionization energy. For each parameter set, two trajectories are shown: one is launched from the Coulomb center, and the other is started in the outer region of configuration space. The spatial extension of the orbits is visualized by the indicated position of the classical ionization saddle point (ISP), which is located at $(13\,100a_0,0,0)$ for an electric field of $E = 3000$ V/m. Due to the classical scaling property the depicted trajectories correspond to one-dimensional manifolds of trajectories with constant parameters ϵ and ω. For each trajectory a view in magnetic-field direction and a side view is shown. With decreasing ϵ the trajectory with the electron launched at the Coulomb center reduces in size and gets chaotic. The outer trajectory with decreasing ϵ completely changes its shape: it avoids more and more the vicinity of the Coulomb center and develops a regular drift motion on an approximately cylindrical shell around the center.

of the Coulomb center. Thus with decreasing ϵ the inner and outer trajectories differ more and more. As a consequence the spatial overlap between outer and inner types of trajectories gets smaller. For $\epsilon=0.0153$ in Fig. 13 no overlap is left at all. In effect, the initial conditions of a trajectory already determine which fraction of the configuration space is covered by the trajectory. The observed behavior can also be seen as a consequence of the fact that with $\epsilon\rightarrow 0$, the z component of the angular momentum, l_z, tends to be conserved, i.e., $\langle l_z^2\rangle-\langle l_z\rangle^2\rightarrow 0$.

Figure 13 and other trajectory calculations clearly show that in the low-ϵ regime, the motion of the electron launched in the outer configuration space is a drift motion around the Coulomb center. This motion is regular and spatially restricted to a more or less cylindrical shell around the Coulomb center, the height, thickness, and other parameters of the shell depending on the individual initial conditions. These drift trajectories are expected to have a quantum analogue which can be called drift states. They seem to play a major role in the ionization process of Rydberg atoms in crossed fields for $\epsilon<0.06$.

It should be noted that for $E=0$ the quantum analogue of the drift trajectories can be obtained in a quite simple way: in this case the Hamiltonian in the symmetric gauge is partially separable, leaving a two-dimensional Hamiltonian with conserved paramagnetic term $(B/2)l_z$, and a potential

$$V=\frac{l_z^2}{2\rho^2}+\frac{B^2}{8}\rho^2-\frac{1}{r} \quad \text{with } \rho^2=x^2+y^2 .$$

For high magnetic field and large l_z, i.e., large centrifugal term, the classically allowed region following from the potential is a quite thin cylindrical shell around the Coulomb center. In the shell the electron performs a rapid oscillation in the ρ direction, and a slow oscillation in the z direction. In the ρ direction, the centrifugal term prevents the electron from entering the central configuration space region. For l_z and B large enough the oscillation frequency in ρ direction approaches the cyclotron frequency. The z oscillation frequency is given by $\rho_0^{-3/2}$ with ρ_0 being the position of the minimum of the ρ potential. For high enough B the z-oscillation frequency is much lower than the cyclotron frequency, and a Born-Oppenheimer separation of the variables ρ and z can be performed. The quantization of the resulting one-dimensional motions can be done semiclassically using the WKB approximation, or the adiabatically separated Schrödinger equation can be solved. The resulting quantum numbers n_ρ and n_z can be used to characterize the drift states by $|n_\rho,n_z,l_z\rangle$. The energy of this state is $(B/2)l_z$ plus the energy of the z oscillation plus the energy of the ρ oscillation. The drift states are realistic for large l_z and B, since in this case the adiabaticity between ρ and z motion is fulfilled, this being the condition of the Born-Oppenheimer approximation. In the low-l_z regime there is no adiabaticity between ρ and z motion, and thus no states $|n_\rho,n_z,l_z\rangle$ exist. In the classical treatment for small values of l_z the increasing influence of the nonlinearity of the Coulomb potential and the loss of adiabaticity between ρ and z motion lead to chaos [2,3].

The trajectories with outer starting points in Fig. 13 for large magnetic fields correspond to a regular drift motion around the core similar to electron orbits in a Penning trap or the electron orbits in our experimental apparatus. The dynamics of an electron in a drift trajectory has three time scales: the fastest being the cyclotron motion, an intermediate one corresponding to the oscillation parallel to the magnetic field, and a very slow $\mathbf{E}\times\mathbf{B}$ drift motion. In a Penning trap the drift motion is called magnetron motion. For a large magnetic field B the diameter of the cyclotron motion of an electron moving far apart from the Coulomb center is so small that the electron essentially is affected by a homogeneous electric field, i.e., locally in properly chosen coordinates $\hat{x}$, $\hat{y}$ and time t the velocity of the electron is

$$\begin{aligned} v_{\hat{x}} &= -v_c\sin(\omega_c t) , \\ v_{\hat{y}} &= \frac{-G}{B}+v_c\cos(\omega_c t) , \end{aligned} \tag{3}$$

where $\mathbf{G}=G\mathbf{e}_{\hat{x}}$ is the local electric field and $\mathbf{B}=B\mathbf{e}_z$. Equation (3) includes the slow drift velocity $(-G/B)\mathbf{e}_{\hat{y}}$ and the rapidly oscillating cyclotron motion. Both components are perpendicular to the magnetic field. The kinetic energy $W_\perp$ perpendicular to the magnetic field, averaged over one cyclotron period, consists of the cyclotron energy $W_c=v_c^2/2$ (in atomic units) which is connected with the oscillating terms in Eq. (3), and the drift energy $W_d=G^2/2B^2$. The drift motion is a fast periodic motion which has an adiabatic invariant proportional to W_c (see also Appendix A). Additionally, if $\epsilon\ll 0.06$, the drift energy W_d can be neglected for an approximate description of the ionization energy, i.e., $W_\perp$ is solely determined by the homogeneous magnetic field. The motion within the intermediate time scale is the oscillation in z direction. The time scale in which the energy of the z oscillation changes is long compared to the frequency ω_z of the z oscillation, and short in comparison to the time scale of the magnetron motion. The z oscillation takes place in a z-dependent potential U with parameters x, y:

$$U_{(x,y)}(z)=-\frac{1}{\sqrt{x^2+y^2+z^2}}-Ex-W+W_\perp , \tag{4}$$

where W is the total energy (usually <0). The potential Eq. (4) goes to zero at the classical turning points of the z oscillations.

For parameters corresponding to the spectra shown in Fig. 6, three electron trajectories in the outer configuration space are depicted in Fig. 14. The electrons, the trajectories of which are represented by thin lines, are launched at a location $(-x_0,0,0)$ with a large value x_0 ($x_0\approx 3500a_0$). The upper trajectory is planar ($z\equiv 0$) and describes an $\mathbf{E}\times\mathbf{B}$ drift motion along an equipotential line. Since there is no z oscillation, the cyclotron energy is quite high, resulting in a large cyclotron radius. The lower trajectories correspond to electrons

with maximum possible energy in the z oscillation, i.e., $W_\perp \approx 0$. In order to show the extension of those three-dimensional trajectories in z direction, in Fig. 14 in addition to the projections onto the $z=0$ plane three-dimensional plots are displayed on the right. The locations where the electron crosses the plane $z \equiv 0$ are indicated by circles. Between successive circles there are many cyclotron cycles; this shows that cyclotron motion and z oscillation can be adiabatically separated. The electron passes the plane $z \equiv 0$ many times as it moves from $(-x_0,0,0)$ towards the ISP; this shows that the drift (i.e., magnetron) motion and z oscillation can be adiabatically separated. The upper three-dimensional trajectory is bound, whereas the lower one is an ionizing trajectory. The latter approaches the Coulomb center closest at its "back side," i.e., opposite to the ISP. The drift trajectories performing wide z oscillations exhibit an important feature: as the electron moves from $(-x_0,0,0)$ towards the ISP, energy is transferred from the z oscillation to the potential energy of the electron in the electric potential (i.e., the potential of external electric and Coulomb field together). This means, although the electron starts quite deeply inside the Coulomb attraction region at $(-x_0,0,0)$, the energy transfer may enable the electron to leave the Coulomb attraction zone, as shown by the lower trajectory in Fig. 14. For fixed distance x_0 there exists a critical energy value above which there are free drift trajectories starting at $(-x_0,0,0)$. With increasing energy in the z oscillation, more energy is transferred to potential energy. Therefore the drift trajectories with maximum energy in the z direction result in the lowest value of the critical energy. If the total energy is given, the trajectory which has maximum energy in the z motion and which is just able to leave the atom determines how closely free classical electrons may approach the Coulomb center.

In order to reduce the numerical effort, it is useful to consider the motion of a "substitute" particle which moves in the plane perpendicular to the magnetic field. The substitute particle motion approximates the projection of the real three-dimensional electron trajectory onto the plane $z=0$, that projection being averaged over a couple of cyclotron periods. Therefore the substitute particle gives information on the projected electron position on time scales larger than the revolution time on a cyclotron orbit. An advantage of the substitute particle is that its equations of motion are faster to integrate than the real electron motion. The substitute particle performs a $\mathbf{D}\times\mathbf{B}$ drift motion, where $\mathbf{D}$ is the time-averaged electric field which acts on the real electron, this average

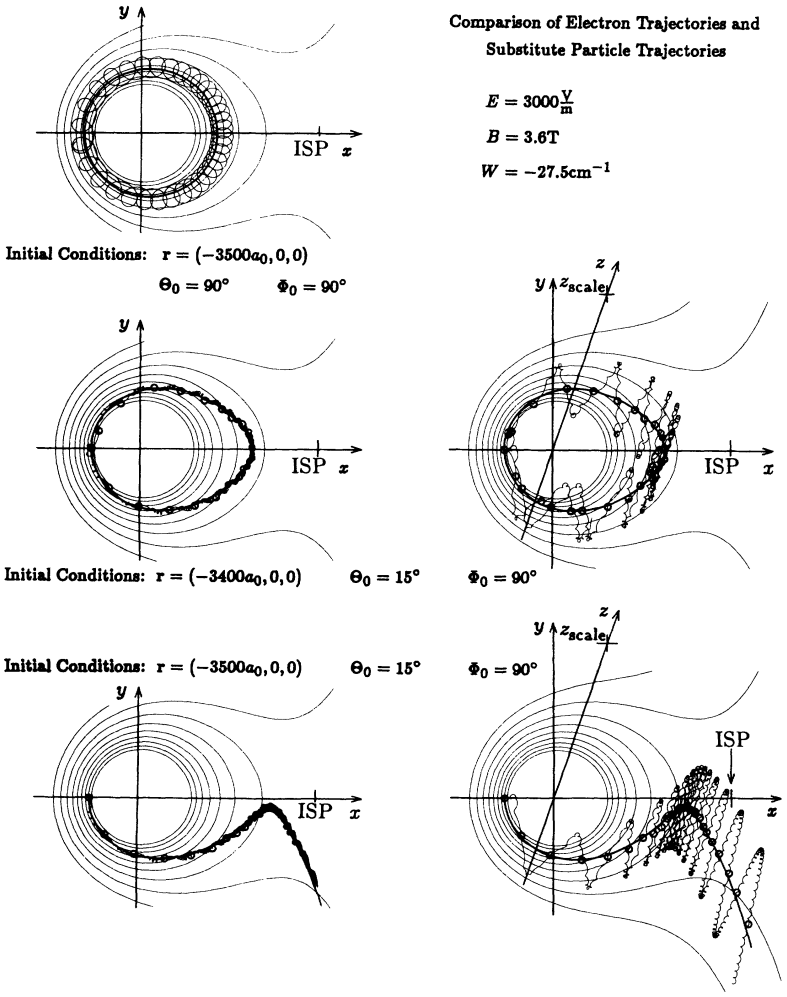

FIG. 14. Drift trajectories with no and maximum energy in the z motion (thin wiggled curves) and with the indicated initial parameters. On the left side the figure shows the trajectories projected onto the $z=0$ plane. The lower two trajectories are also shown in a three-dimensional plot on the right side, whereby the point $(z_{scale},0,0)$ is three times farther away from the origin that the ionization saddle point (ISP). The figure also contains the equipotential lines corresponding to the electric potential $-1/r-Ex$ at energies $W_i = W[1+i(0.15)]$ with $i=0,\ldots,8$ and $z=0$. The points where the trajectories cross the $z=0$ plane are marked by circles. The enhanced curves, which follow those circles, are trajectories of the substitute particle introduced in the text. It can be seen that the substitute particle can be used in order to describe the drift motion of the real electron.

being taken over one z oscillation. Hence the equations of motion of the substitute particle are

$$\dot{x}=D_y/B \ , \quad \dot{y}=-D_x/B \ , \tag{5}$$

with

$$D_x=-E+xf(x,y) \ , \quad D_y=yf(x,y) \ , \tag{6}$$

with the external electric field $\mathbf{E}$ directing in $-x$ direction, and

$$f(x,y)=\int_0^{z_0}\frac{1}{r^3}\frac{1}{\sqrt{-U_{(x,y)}(z)}}dz \Big/ \int_0^{z_0}\frac{1}{\sqrt{-U_{(x,y)}(z)}}dz \ , \tag{7}$$

U taken from Eq. (4) and z_0 being the position of the turning point defined by $U_{(x,y)}(z_0)=0$.

It is also interesting to consider the action integral along one z oscillation which is

$$S_z(x,y)=4\int_0^{z_0}\sqrt{-2U_{(x,y)}(z)}dz \ . \tag{8}$$

By considering a small variation Δx in x and taking the limit $\Delta x \to 0$ it is found that

$$\frac{\partial S_z(x,y)}{\partial x}=4\int_0^{z_0}\frac{\partial}{\partial x}\sqrt{-2U_{(x,y)}(z)}dz$$

$$=4\int_0^{z_0}\frac{E-\frac{x}{r^3}}{\sqrt{-2U_{(x,y)}(z)}}dz \ . \tag{9}$$

The derivative in y direction gives an analogous expression. Since for $z_0-z\to+0$ the integrands are $\sim 1/(\sqrt{z_0-z}\,)$, the integrals are well defined. The variation $\Delta S_z(x,y)$ as a function of Δx and Δy also contains higher order contributions depending on the shift of the integration limit z_0, that being $\Delta z_0 \approx (\partial z_0/\partial x)\Delta x + (\partial z_0/\partial y)\Delta y$. The gradient $\nabla_{(x,y)}S_z(x,y)$ can be recognized to be parallel to $\mathbf{D}$ ($\mathbf{D}$ is the total electric field averaged over one z oscillation). Thus the action S_z does not change along the trajectory of the above introduced substitute particle. This is already a clear indication that S_z becomes important in the semiclassical quantization. However, the conservation of S_z only holds in the regime where $W_\perp=$const can be assumed.

In Fig. 14, the validity of the substitute particle approximation is also demonstrated. The thin electron trajectories have to be compared with the corresponding substitute particle trajectories (thick curves) which were numerically calculated using Eqs. (4)–(7). The projected electron motions $[x(t),y(t),z=0]$ exhibit the expected agreement with the corresponding substitute particle trajectories. Since for the planar electron trajectory (upper trajectory in Fig. 14) the z-averaged electric field equals the electric field in the plane $z=0$, the corresponding substitute particle moves on an equipotential line of the electric potential.

In the high-magnetic-field regime, the atoms are supposed to ionize in the following way (see Fig. 15): according to the above considerations the amplitude of the wave function of the excited Rydberg atoms is usually small beyond the space region which is accessed by classical excited electrons. The excitation energy W determines how far the classically accessed region extends towards the $-x$ direction. We denote this extension by $x_c(W)$. A hypothetical value of the ionization energy is uniquely determined by demanding that a free drift trajectory starting at $(-x_c,0,0)$ must exist. If this is the case, the atom is assumed to ionize via a coupling between the free drift trajectory and the configuration space region which is accessed by classical excited electrons.

It is important to note that this "ionization process"

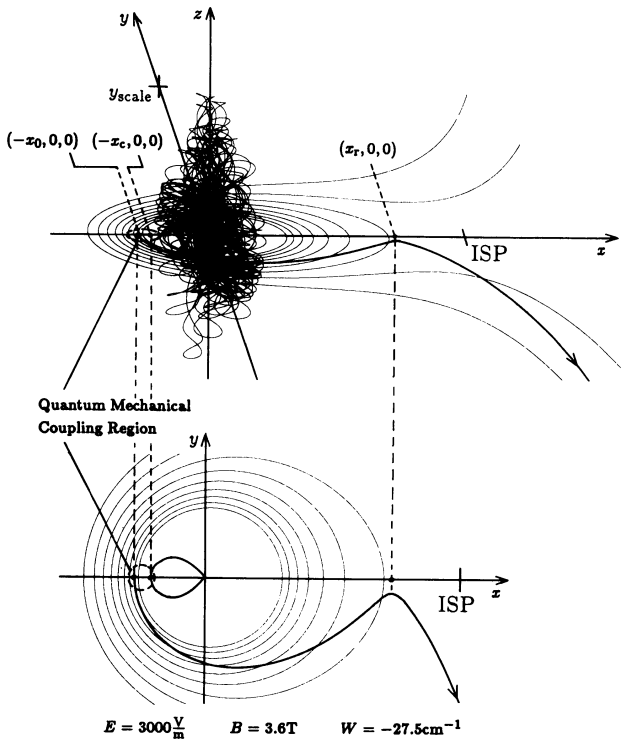

FIG. 15. Description of the ionization process for a small scaled electric field (in this example $\epsilon=0.0153$). The upper plot shows an inner, chaotic trajectory for the indicated energy W, the extension of which coincides with the extension of most wave functions which exist in the vicinity of the indicated set of parameters and can be excited from the ground state. The point y_{scale} is displaced twice as far from the origin as is the ISP. The extension of the space region which is occupied by the chaotic trajectory in the direction opposite to the ISP is denoted by x_c. The value of $x_c(W)$ can be found by an iterative search for the simple planar orbit shown in the lower part of the figure. The enhanced line shows an ionizing substitute particle with the same energy as the chaotic trajectory. The plotted substitute particle trajectory corresponds to an electron drift trajectory with maximum energy in z direction, i.e., among all drift trajectories with equal energy W it exhibits the smallest value of x_0. The value $x_0(W)$ is found by following the substitute particle backwards from $(x_r,0,0)$ to $(-x_0,0,0)$, whereby $(x_r,0,0)$ is defined as the zero of the average electric field, the average taken over one z oscillation. If x_0 does not exceed x_c too much, the excited wave function is weakly coupled to the continuum via free drift states which correspond to the displayed substitute particle trajectory. Thus ionization occurs if $x_c \gtrsim x_0$.

does not happen in classical mechanics because a large momentum kick would be necessary in order to bring the electron from an inner trajectory onto a drift trajectory. However, in quantum mechanics, there is a weak coupling between the inner region $\rho < x_c$ where the excited wave functions have a large amplitude and the quantum mechanical drift states (see Appendixes A and B). This means that this momentum kick occurs with a small probability. The situation is similar to the tunnel effect of a particle through a potential barrier. In the tunnel effect as well as in our problem, a quantum mechanical coupling is required to explain a classically forbidden jump in phase space.

The simple ionization model was tested in the following way: from the experiment shown in Fig. 6, the 90% ionization energy $W_{90\%}$ was taken with the error estimated to be ± 1 cm^{-1}. For $W_{90\%}$ the value x_c was numerically determined. This value, with error bars following from the uncertainty of $W_{90\%}$, is plotted in Fig. 16. For the same energy, substitute particle trajectories with maximum energy in the z direction and zero cyclotron energy were calculated yielding values $x_0(W_{90\%})$ (x_0 is explained in Fig. 15). Since the cyclotron energy was zero, the values $x_0(W_{90\%})$ coincide with the minimum distance which is possible between the Coulomb center and a free classical electron with energy $W_{90\%}$. The values $x_0(W_{90\%})$ are also plotted in Fig. 16. In the upper part of the figure the drift energy W_d was neglected, whereas in the middle of the figure W_d has been taken into account by subtracting $W_d = \langle G_\perp(z)^2 \rangle / 2B^2$ from the energy which is available for the z oscillation [the average is taken over one z oscillation, and $G_\perp(\mathbf{r})$ is the component of the external plus the Coulomb electric field normal to $\mathbf{B}$]. The reduction of the energy in z direction results in an increase of x_0 which becomes evident for $\epsilon > 0.02$. From Fig. 16 it is concluded that in the high-magnetic-field regime ($\epsilon < 0.06$) the ionization model is reasonable. The constant shift between x_c and x_0 may be due to the quantum effects being discussed below. In the low-magnetic-field regime there is an extreme discrepancy between x_0 and x_c. This is no surprise since in that regime the conditions which are necessary in order to make an adiabatic approximation are not fulfilled. The adiabatic separation of the different types of motion is not possible, i.e., the calculated values of x_0 are artificial and do not correspond to really existing drift trajectories. In the lower part of Fig. 16 the most critical adiabatic parameter ω_c/ω_z is plotted for the outer turning point $(x,y)=(x_r,0)$ (see Fig. 15) and for the point $(-x_0,0)$. The z potential associated with a substitute particle trajectory is steepest at $(-x_0,0)$; therefore, at that location, the adiabaticity is worst. Obviously the simple classical model of ionization applies if the adiabaticity parameter ω_c/ω_z exceeds the value of 2 anywhere along the substitute particle trajectory. It is also concluded that for $\omega_c/\omega_z > 2$ quantum states exist which correspond to the drift trajectories.

2. *Quantum mechanical considerations*

Within the adiabatic approximation the classical motion can be quantized in a straightforward way, yielding semiclassical quantum numbers for the three different types of motion (see Appendix A). Due to the adiabaticity between the different types of motion, it is also possible to treat the system quantum mechanically in the framework of a Born-Oppenheimer approximation. The results

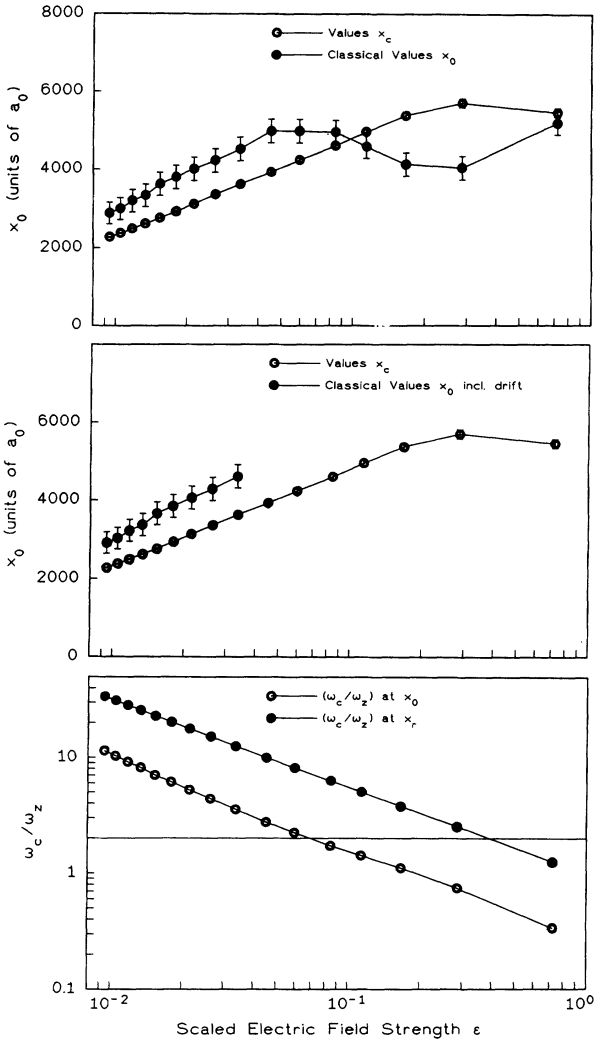

FIG. 16. Test of the classical ionization model described in the text. The energy values used for the calculations are the 90% ionization energies ± 1 cm^{-1} taken from Fig. 8. The values x_c denote the extension of the configuration space volume in $-x$ direction which is accessible to classical electrons starting from the center. In the upper plot these values are compared to values x_0 obtained by calculating the free substitute particle trajectory which penetrates deepest into the Coulomb potential. The error bars result from the uncertainty on the ionization energy. Except for a constant shift there is good agreement for $\epsilon < 0.06$. The values x_0 for $\epsilon > 0.1$ are artificial (see text). In the middle, the energy which is available for the z oscillation was reduced by the amount of the drift energy $W_d = \frac{1}{2}\langle G_1^2 \rangle / B^2$. The drift energy slightly increases x_0, that increase being only evident for $\epsilon > 0.02$. For $\epsilon > 0.04$, the drift energy results in the disappearance of free solutions of the substitute particle equations at the observed 90% ionization energy. The lower part of the figure shows the adiabaticity parameter ω_c/ω_z at the points $(-x_0,0,0)$ and $(x_r,0,0)$ indicated in Fig. 15 (drift energy neglected).

are quantum numbers of one-dimensional motions and corresponding wave functions. Starting with the fastest (i.e., cyclotron) motion, the wave functions corresponding to the fast motion(s) are used as input for the integration of the equations for the slower motions. As described in more detail in Appendix B, one obtains quantum numbers n_c and n_z for the cyclotron motion and the z oscillation. In the case of bound states, an additional quantum number n_m for the drift motion is obtained, whereas free drift states are additionally labeled by the (continuous) value of W. Thus in the high-magnetic-field regime the states can be classified in the following way.

(i) States $|\psi_c\rangle$ which are more or less centered at the Coulomb potential. As already discussed, the extension of these states is approximated by the configuration space volume which is accessible to classical excited electrons. The states $|\psi_c\rangle$ can only be calculated by an exact quantum treatment.

(ii) Bound drift states $|n_c,n_z,n_m\rangle$.

(iii) Free drift states $|n_c,n_z,W\rangle$, whereby W must exceed a continuum threshold W_{n_c,n_z}.

(iv) There exist quantum states which appreciably extend beyond the space region accessible to classical excited electrons, but which also have large amplitude in regions quite close to the Coulomb center where the adiabatic approximation is not possible. The description of these "intermediate" states requires a complete quantum mechanical analysis of the problem which is not given in this paper.

We assume that a state $|\psi_c\rangle$ and a free state $|\psi_s\rangle=|n_c,n_z,W\rangle$ with similar energy W overlap in a small region around $(-x_0,0,0)$. The state $|\psi_c\rangle$ can be thought of as an (approximate) solution of the Schrödinger equation in the inner-configuration-space volume $\rho<x_c+\delta$, with $\rho=\sqrt{x^2+y^2}$, x_c explained in Fig. 15, and δ on the order of $1/\sqrt{B}$. The states $|\psi_c\rangle$ can be found, for example, by solving the pure magnetic-field case for the low-l_z manifolds and treating the weak electric field by perturbation theory. Ionization of $|\psi_c\rangle$ via $|n_c,n_z,W\rangle$ occurs if the coupling term $\langle\psi_c|H|n_c,n_z,W\rangle$ is nonzero. For certain combinations the coupling will be zero due to the discrete symmetries of the Hamiltonian (P_z and TP_y symmetry). However, with the restriction to proper subsets of states the coupling will be nonzero. Based on qualitative approximations of the states $|\psi_s\rangle$ and $|\psi_c\rangle$ in the overlap region, the coupling can be estimated to be very small (this just reflects the fact that in the overlap region the classical momentum vectors corresponding to $|\psi_c\rangle$ and $|\psi_s\rangle$ are perpendicular to each other). Nevertheless, the fact that the coupling is nonzero suffices for ionization. If one assumes $\hbar\to 0$, the coupling matrix element more and more can be considered as a product between plane waves with orthogonal wave vectors. Working that out in more detail reveals that the coupling goes to zero if $\hbar\to 0$. This is consistent with the result that classically, the atoms do not ionize via drift trajectories even if there is a spatial overlap between an inner trajectory and a free drift trajectory with equal energy.

In analogy to Fig. 16, the values x_c and corresponding values x_0 derived from the quantum mechanical drift states are compared in Fig. 17 (see also Fig. 18). The lowest continuum drift state carries the cyclotron zero-point energy. Thus, in order to interpret the experimentally observed ionization energy, it is sufficient to consider drift states in the zeroth Landau band. The cyclotron zero-point energy raises the ionization energy consider-

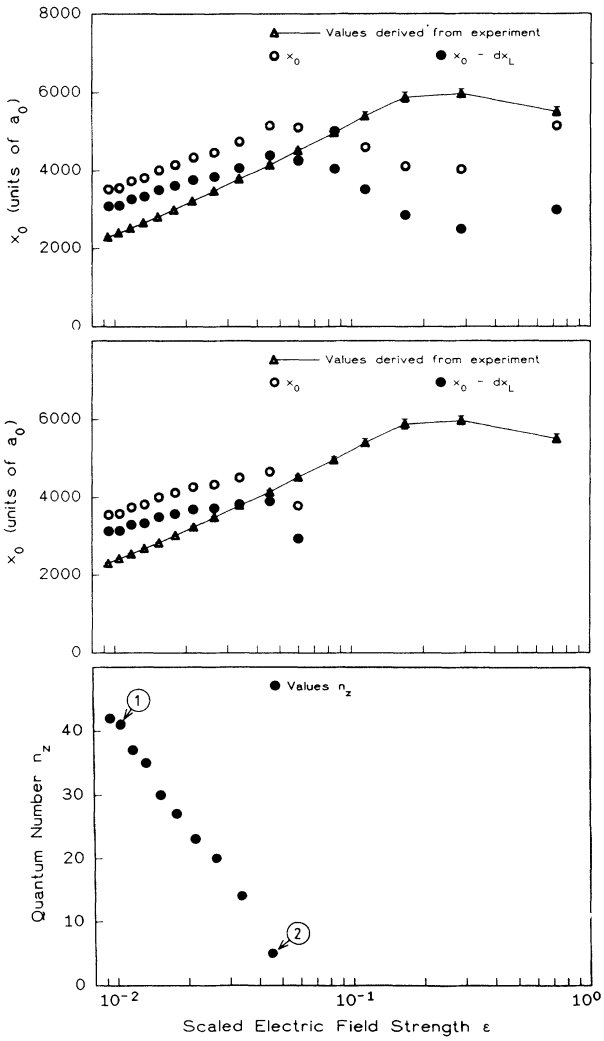

FIG. 17. Test of the semiclassical ionization model described in the text. The comparison between x_c and x_0 is done in analogy to Fig. 16, except that the values x_0 were obtained by searching the quantum drift state which penetrates deepest into the Coulomb potential. Again, as in the classical calculations, results for $\epsilon>0.1$ are artificial. The value $x_0-2/\sqrt{B}$ (i.e., x_0 lowered by the "thickness" of the zeroth Landau state) has also been plotted in the figure. In the uppermost plot the drift energy is neglected, whereas in the plot below this energy has been taken into account. As explained in the text and contrary to classical consideration, x_0 is lowered by the drift energy. The deviations between classical values of x_0 (Fig. 16) and the quantum values shown in this figure result to a large extent from the cyclotron zero-point energy. In the third plot, the values n_z found in the calculations where the drift energy was taken into account are shown. With decreasing ϵ there is a rapid increase of n_z. The labels 1 and 2 indicate the data points for which wave functions are shown in Fig. 18.

ably: in the measurement taken at $B=5.2$ T (Fig. 6) it amounts to 10% of the observed ionization energy $|W_{\text{ion}}|$. In the calculation the quantum number n_z is first determined. This is done by calculating z-wave functions for different n_z at and inside the ISP along the positive x axis (i.e., the ISP side). The averaging of the z potential in $\tilde{x}$ direction [see Appendix B, Eq. (B2)] was not performed, since for large B this only gives minor corrections. The wave function with the lowest value n_z which has an average electric field in the negative x direction corresponds to the lowest continuum drift state. Since n_z is a good quantum number of the drift states, the z-wave function is also identified by n_z at the left turning point $(-x_0,0)$. This condition is utilized to fix the value of x_0. In the upper plot of Fig. 17, the drift energy W_d is neglected, whereas in the plot below it has been taken into account. Since the "thickness" of the drift states in the lowest Landau band is $\sim 2/\sqrt{B}$, ionization may already occur if $x_0-x_c\sim 2/\sqrt{B}$. Therefore the values $x_0-2/\sqrt{B}$ are also shown in Fig. 17. As in the classical considerations the model only makes sense for $\epsilon<0.06$. In this regime, there is qualitative agreement between the values x_0 and x_c. Deviations may arise from the most obvious imperfection of the idealized model: the fact that with increasing ϵ the adiabaticity ω_c/ω_z gets worse must be expected to cause effects already for $\epsilon\approx 0.06$, where drift states start to exist: at $\epsilon\approx 0.06$ there will be diabatic couplings between drift states with different adiabatic quantum numbers. This higher order coupling would lower the values of x_0. In particular, the states $|\psi_c\rangle$ may also be indirectly coupled to free drift states via the above so-called "intermediate" states. The mentioned effects would explain why, in Fig. 17, the values of x_0 are larger than x_c in the relevant range of ϵ.

Finally it also has to be noticed that in principle, the infinite mass approximation of the Coulomb center cannot be applied if the electron has left its attraction zone. However, the electron motion is much faster than the motion of the Rb^+ ion. During the time which a classical electron needs to travel from $(-x_0,0,0)$ to the ISP the Rb^+ ion typically travels about $50a_0$. Thus the inclusion of the Rb^+ motion should not change the results concerning the ionization process. An influence on the energy spectrum, however, must be expected. In the case of hydrogen, where the mentioned value of $50a_0$ would have to be multiplied by 85, there may even be an influence on the ionization behavior.

In conclusion of this subsection, it can be stated that in the high-magnetic-field regime ($\epsilon<0.06$) the presented model of ionization at least qualitatively reproduces the experimentally observed ionization energy.

B. Low-magnetic-field regime

The discussion of the high-magnetic-field case showed that the adiabaticity parameter ω_c/ω_z is of crucial importance when constructing the drift states. In the low-magnetic-field regime $\epsilon>0.06$, the adiabaticity between cyclotron motion and z oscillation is lost. This provides an argument why for $\epsilon>0.06$ the ionization energy increases again: the drift states which lead to ionization simply do not exist anymore.

For $B\approx 0$, it is reasonable to assume that ionization occurs similar to the magnetic-field-free case: in the classical picture the electron is excited at the core and directly propagates into the continuum. Trajectory calculations reveal that for $\epsilon>1.5$, this direct-path ionization explains the experimentally observed ionization threshold which in this regime does not deviate significantly from the zero magnetic-field ionization energy.

More interesting is the range $1.5\gtrsim\epsilon\gtrsim 0.2$, the lower bound being determined by the ionization energy maximum. In this regime, the experimentally observed ionization energy is well below the energy value above which classical direct-path ionization would be possible. As in the case $\epsilon<0.06$, the ionization should occur via free states which spatially overlap with the configuration space region accessible to classical electrons starting at the Coulomb center. From Fig. 16, it is clear that the adiabatic conditions are reasonably well fulfilled in the vicinity of and beyond the ISP. This is easy to understand since with increasing distance from the Coulomb center both the z electric field (which is exclusively caused by the Coulomb electric field) and ω_z decrease. For example, at the ISP the adiabatic parameter ω_c/ω_z is equal to 1 for $\epsilon=1$. Thus as $\epsilon\lesssim 1$ one can expect continuum drift states corresponding to the classical trajectory depicted in Fig. 19. This trajectory is similar to the outer part of the free drift trajectories which exist for $\epsilon<0.06$ (see Fig. 14). The difference is that in the high-ϵ regime, the trajectory does not exhibit the features of a drift trajectory any more if it is continued inside the ISP (due to the lack of adiabaticity). In the following, it is assumed that ionization takes place via a coupling between the configuration space region accessible to classical excited

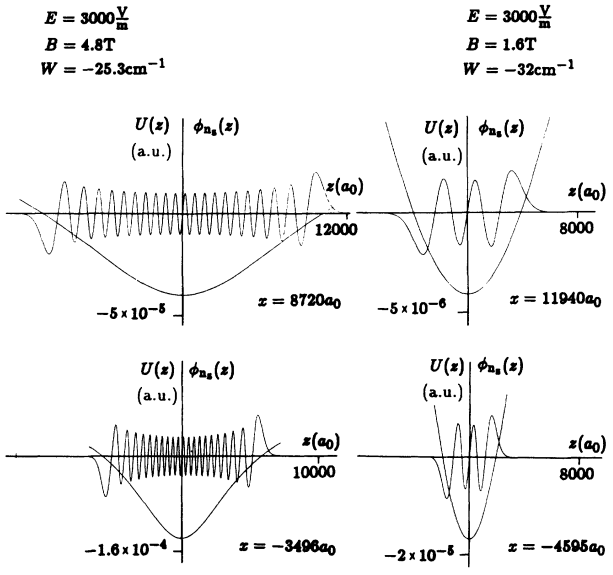

FIG. 18. The figure shows z-wave functions for $y=0$ and two values of x. The plots to the left (right) correspond to the data point labeled by 1 (2) in Fig. 17. The negative value of x corresponds to $(x,y)=(-x_0,0)$, the positive value to $(x_r,0)$ (see Fig. 15). Since the wavelength of the z wave function at $(x_r,0)$ is larger than the wavelength at $(x_0,0)$, the adiabaticity is less fulfilled for $(-x_0,0)$ than for $(x_r,0)$.

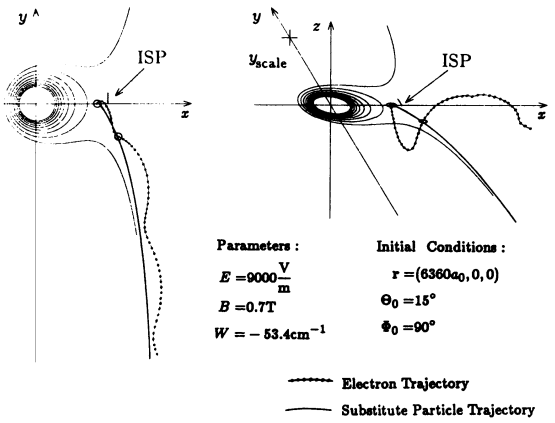

FIG. 19. Low-B escaping trajectory. In the regime $\epsilon<1.5$ one finds free drift trajectories starting in the vicinity of the classical ionization saddle point (ISP). The depicted electron trajectory corresponds quite well to the associated substitute particle trajectory. In the three-dimensional plot the point $(y_{\text{scale}},0,0)$ is two times farther away from the origin than the ISP.

electrons and continuum states corresponding to the trajectory depicted in Fig. 19 which do not approach the Coulomb center much closer than the ISP.

At the actually observed ionization energy, the extension x_c of trajectories towards the ISP is numerically determined. For the free drift trajectories beyond the ISP, it is again found that maximum energy in the z oscillation leads to minimum distance to the Coulomb center. The minimum distance $x_r(x_r>0)$ is determined via the condition that the average electric-field component $\mathbf{D}$, the average being taken over the z oscillation, has a zero at $(x,y)=(x_r,0)$. The values x_r have to be compared to x_c, as done in Fig. 20. For $\epsilon>0.2$ the agreement is reasonable. Similar to the discussion of the high-magnetic-field case, the model can be extended towards a quantum mechanical description. However, since this would not bring any further insight, these considerations are not presented.

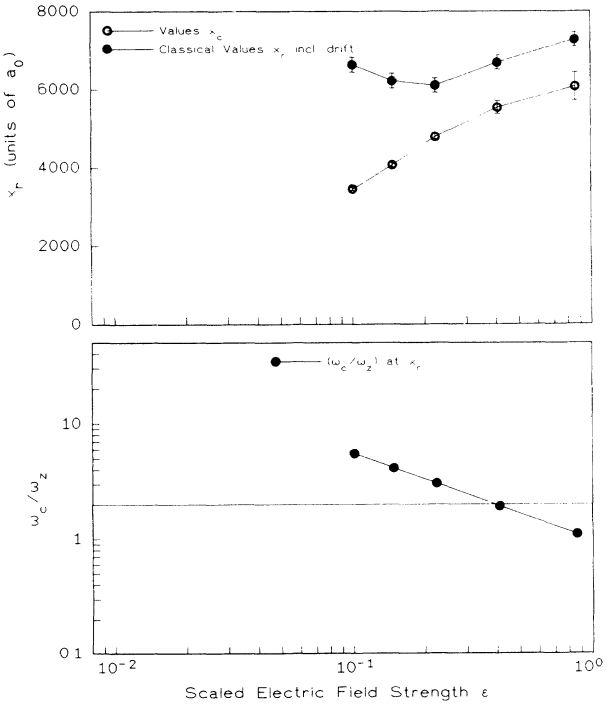

FIG. 20. Classical test of the ionization model for $\epsilon>0.2$. The experimental parameters were taken from Fig. 7. The value x_c which describes the maximum extension of trajectories launched at the center towards the ISP is found numerically. In the calculation of x_r, the drift energy $W_d=\frac{1}{2}(\langle G_1^2\rangle/B^2)$ has been included; however, this has little effect since x_r is defined by $\langle G_1\rangle=0$. For $\epsilon>0.2$, x_c and x_r qualitatively agree. The adiabaticity parameter at $(x_r,0)$ is shown in the lower part of the figure.

In the transition region between low and high magnetic field $(0.2>\epsilon>0.06)$ the configuration space region where the adiabaticity parameter satisfies $\omega_c/\omega_z>1$ gradually increases. In order to explain the gradual decrease of the ionization energy between the ionization energy maximum and the minimum, one could speculate about the existence of "incomplete" drift state wave functions, which would have large amplitude only at locations where ω_c/ω_z is high enough. Such states would be X shaped, the X centered on the x axis in the vicinity of the ISP. More precise statements in this ϵ regime require an exact quantum mechanical treatment.

V. CONCLUSION

In this paper an experimental apparatus was presented which allows one to record spectra of Rydberg atoms in crossed fields, simultaneously below and above the ionization energy. Experimental results on the ionization energy and the width of the ionization curve are shown. The ionization energy as a function of the scaled electric-field strength exhibits a pronounced maximum at $\epsilon=0.19$. The ionization energy in the regimes $\epsilon>0.2$ and $\epsilon<0.06$, i.e., the regimes where the ionization energy increases with the magnetic field, was explained by electron states which correspond to different types of classical drift motions of electrons in the outer-configuration-space region.

ACKNOWLEDGMENTS

The authors would like to thank P. F. O'Mahony for many valuable discussions.

APPENDIX A: SEMICLASSICAL QUANTIZATION OF THE DRIFT TRAJECTORIES

The classical action integral $\int \mathbf{p}\cdot d\mathbf{q}$ of a drift trajectory (B large enough) over a certain time can be split up into different contributions each being associated with a semiclassical quantum number. For low ϵ and sufficiently large distance from the Coulomb center, the classical motion $\mathbf{r}(t)$ can be written as $\mathbf{r}(t)=z(t)\mathbf{e}_z+\mathbf{r}_c(t)+\mathbf{r}_d(t)$, whereby $\mathbf{r}_c(t)$ describes the fast circular drift motion $(r_{c,z}\equiv 0)$, $z(t)\mathbf{e}_z$ the z oscillation which takes place on the intermediate time scale, and $\mathbf{r}_d(t)$ the drift motion which exhibits the slowest time scale and which is also two dimensional $(r_{d,z}\equiv 0)$. The drift motion $\mathbf{r}_d(t)$ has to be

identified with the motion of the substitute particle discussed in the text. The action integral becomes

$$\int \mathbf{p}\cdot d\mathbf{q}=\int \mathbf{p}_\perp\cdot d\mathbf{q}_\perp+\int p_z dz \ . \tag{A1}$$

We use $\mathbf{p}=\mathbf{v}-\mathbf{A}(\mathbf{x})$, decompose $\mathbf{r}(t)$ in the above-mentioned way, take into account that $\mathbf{A}$ is a linear function of the coordinates, apply Stokes law, and use $\mathbf{B}=rot\ \mathbf{A}$ to obtain the action integral over one magnetron period T_d,

$$\begin{aligned}\int_{T_d}\mathbf{p}\cdot d\mathbf{q}=&\int_{T_d}v_c^2dt-\int_{T_d}\mathbf{A}(\mathbf{r}_c)\cdot d\mathbf{r}_c+\int_{T_d}v_z^2(t)dt\\&+\oint_{T_d}\frac{D^2(t)}{B^2}dt+BF_d\\&+\int_{T_d}[2\mathbf{v}_c(t)\cdot\mathbf{v}_d(t)-\mathbf{v}_d(t)\cdot\mathbf{A}(\mathbf{r}_c(t))\\&\quad-\mathbf{v}_c(t)\cdot\mathbf{A}(\mathbf{r}_d(t))]dt \ ,\end{aligned} \tag{A2}$$

where $\mathbf{D}$ is the electric field averaged over one z oscillation [see Eq. (6)], and F_d is the area enclosed by $\mathbf{r}_d(t)$. All the terms in the last integral of Eq. (A2) are neglected because they are rapidly oscillating [with $\sin(\omega_c t)$]. The other terms in Eq. (A2) are grouped as action integrals of periodic motions with different time scales. In the adiabatic approximation each action integral integrated over the corresponding oscillation period is an adiabatic invariant. The cyclotron integral is

$$S_c=\oint_{T_c}v_c^2dt-BF_c=\frac{2\pi}{B}\frac{v_c^2}{2} \ , \tag{A3}$$

where $F_c=\frac{\pi}{B^2}v_c^2$ is the area inside a cyclotron circle. Equation (A3) simply means that the cyclotron energy W_c is constant. The z motion yields the adiabatic invariant

$$S_z=\oint_{T_z}v_z^2dt \ , \tag{A4}$$

which is identical to Eq. (8). Finally the drift motion corresponds to the adiabatic invariant

$$S_m=\oint_{T_d}\frac{D^2(t)}{B^2}dt+BF_d \ . \tag{A5}$$

A test of whether the adiabatic separation is done correctly is to check whether in the limit of the external electric field $E\to 0$ the well-known constant of motion l_z in the symmetric gauge can be recovered as a linear combination of the values S_c and S_m. This is possible: in the case of large B and l_z, we get $l_z=1/2\pi\ (S_c-S_m)$.

With the known adiabatic invariants, the system is semiclassically quantized by $S_c=2\pi(n_c+\frac{1}{2})$, $S_z=2\pi(n_z+\frac{1}{2})$, and $S_m=2\pi n_m$. Appendix B shows that it is not necessary to include a zero-point value π of the action S_m.

APPENDIX B: ADIABATIC SEPARATION OF THE SCHRÖDINGER EQUATION

The local Hamiltonian at a given point (x,y,z) in the outer configuration space of the system of interest is investigated. For the calculation of the cyclotron wave function the local electric field in the vicinity of (x,y,z) is assumed to be homogeneous: $\mathbf{G}=(G_x,G_y,G_z)$. Then the coordinate system is rotated in such a way that the electric field $\mathbf{G}_\perp$ perpendicular to the magnetic field directs in $\tilde{x}$ direction. Additionally $(x,y,0)$ is chosen as new origin. In the coordinates $(\tilde{x},\tilde{y},z)$ (note that z did not change) and with $G_\perp=\sqrt{G_x^2+G_y^2}$ the local Hamiltonian in the gauge $\mathbf{A}=(0,B\tilde{x},0)$ is

$$H_c=\tfrac{1}{2}(\tilde{p}_x^2+\tilde{p}_y^2)+B\tilde{x}\tilde{p}_y+\frac{B^2}{2}\tilde{x}^2+G_\perp\tilde{x}+\tfrac{1}{2}p_z^2+G_z z \ . \tag{B1}$$

The motion transverse to $\mathbf{B}$ [upper line in Eq. (B1)] and the z motion separate (this results from the assumption of locally constant electric field $\mathbf{G}$). The Hamiltonian Eq. (B1) conserves $\tilde{p}_y$. The remaining one-dimensional motion in $\tilde{x}$ direction takes place in an oscillator potential with frequency B, which equals the cyclotron frequency (in atomic units), the potential minimum located at $\tilde{x}_s=(-G_\perp-B\tilde{p}_y)/B^2$. The cyclotron energy levels are $W_c=B(n_c+\frac{1}{2})$ which correspond to the semiclassical quantization condition for the classical adiabatic invariant S_c. According to the Born-Oppenheimer approximation a quantum mechanical drift state has a good quantum number n_c. The wave functions in $\tilde{x}$ direction, i.e., in direction of the local electric field $\mathbf{G}$, are the well-known Landau functions centered at the value $\tilde{x}_s$. The square of the lowest one falls off proportional to $\sim\exp[-B(\tilde{x}-\tilde{x}_s)^2]$, i.e., the "thickness" of the drift states in the lowest Landau band is on the order of $1/\sqrt{B}$. Due to the symmetry of the Landau functions the velocity in $\tilde{y}$ direction, $\tilde{v}_y$, is $\langle\tilde{v}_y\rangle=\langle\tilde{p}_y+B\tilde{x}\rangle=\tilde{p}_y+B\tilde{x}_x=-G_\perp/B$ which is the classical drift velocity. For a cyclotron wave function centered at (x,y,z), i.e., $\tilde{x}_s=0$, $\tilde{p}_y=-G_\perp/B$ has to be chosen.

The z-wave function $\phi_{n_z,x,y}(z)$ is calculated for fixed cyclotron energy $W_c=B(n_c+\frac{1}{2})$ at fixed coordinates (x,y). The potential $V_{(n_c,x,y)}$ for the z-wave function is obtained via averaging the potential Eq. (4) over the already known cyclotron wave function $\psi_{n_c,x,y,z}(\tilde{x})$, where $\tilde{x}$, $\tilde{y}$ are the above introduced local coordinates at (x,y,z):

$$\begin{aligned}V_{(n_c,x,y)}(z)=&\int_{\tilde{x}=-\infty,\tilde{y}\equiv 0}^{\tilde{x}=\infty}\left[-\frac{1}{\sqrt{x'^2+y'^2+z^2}}-Ex'\right]\\&\times|\psi_{n_c,x,y,z}(\tilde{x})|^2d\tilde{x} \ .\end{aligned} \tag{B2}$$

The values x', y' are coordinates in the usual coordinate system, and are obtained by retransforming from the local coordinate system associated with the point (x,y,z).

WKB quantization or solution of the one-dimensional Schrödinger equation in the potential Eq. (B2) yields z-wave functions $\phi_{n_c,n_z,x,y}(z)$ and energy values $W_z(n_c,n_z)$ which depend on the coordinates (x,y). In the Born-Oppenheimer approximation, n_z is a good quantum number and can be identified with the value of S_z [see Eqs. (8) and (A4)]. In the WKB approximation the energy $W_z(n_c,n_z)$ is found by

$$S_z = 2\pi\hbar(n_z+\tfrac{1}{2}) = 4\int_0^{z_0[W_z(n_c,n_z)]} \sqrt{W_z(n_c,n_z)-V_{n_c,n_z,x,y}(z)}\,dz \ , \quad \text{(B3)}$$

whereby $z_0(W_z)$ is the classical turning point in the potential $V_{n_c,n_z,x,y}(z)$. For large magnetic-field values the dependence of $W_z(n_c,n_z)$ on n_c is very weak. The sum energy $W_c(n_c)+W_z(n_c,n_z)+W_d(n_c,n_z)$ is the total energy W, whereby the drift energy W_d is much smaller than the other contributions. Solutions fulfilling this boundary condition are found on curves in the $z=0$ plane, which can be labeled by the quantum numbers n_c and n_z. For simplicity in the following each curve will be identified with a "state" $|n_c,n_z\rangle$. The analogues of those curves in the classical considerations are the substitute particle trajectories. At each point along the curves the electrons have a certain velocity parallel to the curve which follows from the actual electric field $\mathbf{G}$ averaged over the fast motions, denoted by $\tilde{\mathbf{D}}(x,y)$:

$$\tilde{\mathbf{D}}(x,y)=\int_{z=-\infty}^{\infty}\int_{\bar{x}=-\infty,\bar{y}\equiv 0}^{\bar{x}=\infty}\mathbf{G}(x',y',z)|\phi_{n_c,n_z,x,y}(z)|^2 \times|\psi_{n_c,x,y,z}(\bar{x})|^2 dz d\bar{x} \ , \quad \text{(B4)}$$

where $\mathbf{G}(\mathbf{r})$ is the sum of external and Coulomb electric field. Due to the symmetry of $\mathbf{G}(x,y,z)$ and $\phi_{n_c,n_z}(z)$, $\tilde{\mathbf{D}}(x,y)$ is perpendicular to $\mathbf{B}$. It should also be perpendicular to the curve $|n_c,n_z\rangle$ since this curve corresponds to the magnetron drift resulting from $\tilde{\mathbf{D}}(x,y)$. For $\epsilon<0.06$ it was found numerically that $\tilde{\mathbf{D}}(x,y)$ is perpendicular to the corresponding curve $|n_c,n_z\rangle$ in fact to a good approximation. The situation gets worse for $\epsilon>0.06$; however, in this regime the key feature, which is the adiabaticity, gets lost anyway.

The magnetron motion is considered in curved coordinates u,v which are adapted to the curves $|n_c,n_z\rangle$. The direction perpendicular to the curve $|n_c,n_z\rangle$ gives the coordinate u, the length along $|n_c,n_z\rangle$ will be called v. In order to get a quantization condition for the magnetron motion, the phase accumulation of the magnetron wave function along $u\equiv 0$ can be calculated. As already mentioned, the drift velocity $[\tilde{\mathbf{D}}(v)\times\mathbf{B}]B^2$ to a good approximation is parallel to the direction e_v. Thus the infinitesimal phase accumulation of the wave function in v direction is $d\alpha=[\tilde{D}(v)/B]dv-\mathbf{A}(x(v),y(v))d\mathbf{v}$. The total phase accumulation along the curve $|n_c,n_z\rangle$ is the curve integral

$$S_{|n_c,n_z\rangle}=\oint_{|n_c,n_z\rangle}\frac{\tilde{D}(v)}{B}dv-\oint_{|n_c,n_z\rangle}\mathbf{A}(x,y)\cdot d\mathbf{v} = \oint_{|n_c,n_z\rangle}\frac{\tilde{D}(v)}{B}dv+BF_{|n_c,n_z\rangle} \ , \quad \text{(B5)}$$

where $F_{|n_c,n_z\rangle}$ is the area inside the closed curve $|n_c,n_z\rangle$. Since the phase accumulation must be an integer times 2π, the magnetron quantization condition is analogous to Eq. (A5),

$$S_{|n_c,n_z\rangle}=n_m 2\pi \ . \quad \text{(B6)}$$

The gauge independence of the results should be explicitly noted. Since the total energy W is uniquely determined by Eq. (B6), the quantization based on the Born-Oppenheimer approximation is complete: the spectrum is obtained by calculating the energy values of the states $|n_c,n_z,n_m\rangle$.

There are also ionizing drift states which correspond to the lower trajectory depicted in Fig. 14. They do not have to fulfill the magnetron condition Eq. (B6). Thus in this case there is no quantization by which only distinct curves $|n_c,n_z\rangle$ are physical. Each number set (n_c,n_z) has a continuous spectrum of free drift states $|n_c,n_z,W\rangle$, whereby the energy W must exceed the ionization threshold W_{n_c,n_z} associated with n_c and n_z. The ionization threshold W_{n_c,n_z} increases with n_c, and decreases with n_z. It should be noted that the drift energy can be iteratively taken into account by adding the average drift energy $\langle G_\perp^2/2B^2\rangle$ to the potential Eq. (B2), [averaging integral analogous to Eq. (B4)].

[1] J. B. Delos, S. K. Knudson, and D. W. Noid, Phys. Rev. A **30**, 1208 (1984).
[2] G. Wunner, U. Woelk, I. Zech, G. Zeller, T. Ertl, F. Geyer, W. Schweitzer, and H. Ruder, Phys. Rev. Lett. **57**, 3261 (1986).
[3] G. Wunner and H. Ruder, Phys. Scr. **36**, 291 (1987).
[4] H. Friedrich and D. Wintgen, Phys. Rep. **183**, 37 (1989).
[5] D. Delande, A. Bommier, and J. C. Gay, Phys. Rev. Lett. **66**, 141 (1991).
[6] P. F. O'Mahony and F. Mota-Furtado, Phys. Rev. Lett. **67**, 2283 (1991).
[7] S. Watanabe and H. Komine, Phys. Rev. Lett. **67**, 3227 (1991).
[8] M. H. Halley, D. Delande, and K. T. Taylor, J. Phys. B **25**, L525 (1992).
[9] J. Main and G. Wunner, Phys. Rev. Lett. **69**, 586 (1992).
[10] A. Holle, G. Wiebusch, J. Main, B. Hager, H. Rottke, and K. H. Welge, Phys. Rev. Lett. **56**, 2594 (1986).
[11] J. Main, G. Wiebusch, A. Holle, and K. H. Welge, Phys. Rev. Lett. **57**, 2789 (1986).
[12] G. Wiebusch, J. Main, K. Krüger, H. Rottke, A. Holle, and K. H. Welge, Phys. Rev. Lett. **62**, 2821 (1989).
[13] G. Raithel, M. Fauth, and H. Walter, Phys. Rev. A **44**, 1898 (1991).
[14] C. Iu, G. R. Welch, M. M. Kash, L. Hsu, and D. Kleppner, Phys. Rev. Lett. **63**, 1133 (1989).
[15] W. R. S. Garton and F. S. Tomkins, Astrophys. J. **158**, 839 (1969).
[16] A. R. Edmonds, J. Phys. (Paris) Colloq. **31**, C4-71 (1970).
[17] A. F. Starace, J. Phys. B **6**, 585 (1973).
[18] D. Wintgen and H. Friedrich, Phys. Rev. A **36**, 131 (1987).
[19] D. Wintgen, Phys. Rev. Lett. **61**, 1803 (1988).

[20] M. L. Du and J. B. Delos, Phys. Rev. A **38**, 1896 (1988).
[21] M. L. Du and J. B. Delos, Phys. Rev. A **38**, 1913 (1988).
[22] M. C. Gutzwiller, Physica D **5**, 183 (1982).
[23] M. Berry, in *Chaotic Behaviour of Deterministic Systems,* Les Houches Session 36, edited by G. Iooss, R. H. G. Helleman, and R. Stora (North-Holland Publishing Company, Amsterdam, 1983).
[24] E. J. Heller, Phys. Rev. lett. **53**, 1515 (1984).
[25] E. B. Bogomolny, Physica D **31**, 169 (1988).
[26] D. Wintgen and A. Hoenig, Phys. Rev. Lett. **63**, 1467 (1989).
[27] G. Raithel, M. Fauth, and H. Walther, Phys. Rev. A **47**, 419 (1993).